ARTICLE

Determinants of ion selectivity in ASIC1a- and ASIC2a-containing acid-sensing ion channels

Timothy Lynagh[1]* , Emelie Flood[2]* , Céline Boiteux[2] , Zeshan Pervez Sheikh[1] , Toby W. Allen[2], and Stephan A. Pless[1]

Trimeric acid-sensing ion channels (ASICs) contribute to neuronal signaling by converting extracellular acidification into excitatory sodium currents. Previous work with homomeric ASIC1a implicates conserved leucine (L7′) and consecutive glycine-alanine-serine (GAS belt) residues near the middle, and conserved negatively charged (E18′) residues at the bottom of the pore in ion permeation and/or selectivity. However, a conserved mechanism of ion selectivity throughout the ASIC family has not been established. We therefore explored the molecular determinants of ion selectivity in heteromeric ASIC1a/ASIC2a and homomeric ASIC2a channels using site-directed mutagenesis, electrophysiology, and molecular dynamics free energy simulations. Similar to ASIC1a, E18′ residues create an energetic preference for sodium ions at the lower end of the pore in ASIC2a-containing channels. However, and in contrast to ASIC1a homomers, ion permeation through ASIC2a-containing channels is not determined by L7′ side chains in the upper part of the channel. This may be, in part, due to ASIC2a-specific negatively charged residues (E59 and E62) that lower the energy of ions in the upper pore, thus making the GAS belt more important for selectivity. This is confirmed by experiments showing that the L7′A mutation has no effect in ASIC2a, in contrast to ASIC1a, where it eliminated selectivity. ASIC2a triple mutants eliminating both L7′ and upper charges did not lead to large changes in selectivity, suggesting a different role for L7′ in ASIC2a compared with ASIC1a channels. In contrast, we observed measurable changes in ion selectivity in ASIC2a-containing channels with GAS belt mutations. Our results suggest that ion conduction and selectivity in the upper part of the ASIC pore may differ between subtypes, whereas the essential role of E18′ in ion selectivity is conserved. Furthermore, we demonstrate that heteromeric channels containing mutations in only one of two ASIC subtypes provide a means of functionally testing mutations that render homomeric channels nonfunctional.

Introduction

Acid-sensing ion channels (ASICs) are ligand-gated cation-permeable channels expressed in the cell membrane throughout the nervous system (Wemmie et al., 2013). Upon extracellular acidification, protonation of the extracellular domain leads to activation of the membrane-spanning channel, and excitatory current through ASICs contributes to synaptic signaling, nociception, and excitotoxicity (Wemmie et al., 2013). Excitatory function derives from ~10-fold greater permeability of Na^+ than K^+ ions through the channel pore (Kellenberger and Schild, 2015). Rodents and humans possess four ASIC genes (*ASIC1–ASIC4*) encoding six subunits (ASIC1a, -1b, -2a, -2b, -3, and -4), which assemble into homo- or heterotrimeric channels (Wemmie et al., 2013). ASIC1a-containing channels are highly expressed in the central nervous system, and recombinantly expressed ASIC1a homomers are have been studied intensely (Jasti et al., 2007; Waldmann et al., 1997; Wemmie et al., 2013). These structural and functional data have provided some insight into the molecular basis for Na^+ selectivity

in ASIC1a (Baconguis et al., 2014; Lynagh et al., 2017a), but the precise mechanism throughout the family remains unclear.

The x-ray structure of chick ASIC1 (cASIC1) in the presence of MitTx, an irreversible toxin agonist (PDB accession no. 4NTW), seems to have captured an open state, suggested by the presence of a bound Cs^+ ion in the middle of the pore in Cs^+-soaked crystals (Baconguis et al., 2014). Little is known about whether permeating ions enter and exit through lateral pathways near the upper part of the pore or whether they pass the length of the central cavity of the extracellular domain. Ion selectivity, however, seems to derive from several residues in the pore-lining, second membrane-spanning helix (M2) of ASIC1a subunits, which, for better comparison, can be numbered from 0′ near the top of the pore to 21′ at the intracellular end of the pore (Fig. 1). D0′ side chains, conserved in most but not all ASICs, skirt the upper vestibule of the pore, and the D0′N substitution decreases Na^+ conductance but has little effect on the relative permeability

profile of monovalent cations ($P_{Li+} \approx P_{Na^+} > P_{K^+} > P_{Cs^+}$; Yang and Palmer, 2014). At the middle of M2, the highly conserved residues G10′, A11′, and S12′ play an intricate role in channel function. G10′A/C and S12′A/C substitutions render ASIC1a nonfunctional (Carattino and Della Vecchia, 2012; Li et al., 2011; Yang et al., 2009), and x-ray structures of cASIC1 show these residues at the narrowest part of the pore, either as straight helices (Baconguis and Gouaux, 2012; Jasti et al., 2007) or as unwound segments that form a glycine-alanine-serine (GAS) belt (Fig. 1 A; Baconguis et al., 2014; Yoder et al., 2018). Recent experimental and computational data suggest that although the GAS belt is not the primary determinant of ion selectivity in ASIC1a, it contributes to a large energy barrier in the middle of the pore, along with flanking L7′ and L14′ residues, which are highly conserved and whose mutation dramatically decreases Na$^+$ selectivity (Lynagh et al., 2017a). The most notable control over selective Na$^+$ conduction through ASIC1a is a band of carboxylate side chains at the bottom of the pore, formed by E18′ and D21′, which confers substantial preference for Na$^+$ over K$^+$ (Lynagh et al., 2017a). However, the magnitude of this preference depends heavily on the structure of the lower end of the pore (Lynagh et al., 2017a). Here, the resolution of structural data is lower than for other parts of the protein (Baconguis and Gouaux, 2012; Yoder et al., 2018), and it is unknown if the shape of the pore is conserved across different ASIC subtypes. Certainly, and despite its conservation, E18′ seems less important for Na$^+$ conduction in structurally related epithelial Na$^+$ channels (ENaCs; Yang and Palmer, 2018), in which mutations in the GAS belt (or equivalent 10′–12′ residues) affect ion selectivity more directly (Kellenberger et al., 1999) than in ASIC1a.

The molecular determinants of ion selectivity have been explored little in ASIC2-, ASIC3-, and ASIC4-containing channels, which also play important roles in the nervous system (Gründer and Pusch, 2015; Paukert et al., 2004; Wemmie et al., 2013) and which could shed light on the broader mechanisms of Na$^+$ selectivity among ASIC channels. In seeking to dissect conserved features of ion selectivity in ASICs, we measured ion selectivity via relative permeability profiles calculated from reversal potentials in ASIC2a homomers and ASIC1a/ASIC2a heteromers containing mutations in the M2 helix. Additionally, we performed MD free energy simulations with vertebrate ASIC2a homomers and ASIC1a/ASIC2a heteromers modeled on the cASIC1 x-ray structure (PDB accession no. 4NTW; Baconguis et al., 2014).

Materials and methods

Molecular biology, two-electrode voltage-clamp experiments, and data analysis

cDNA plasmids used were mouse ASIC1a (mASIC1a) in the pSP64 vector (provided by Marcelo Carattino, University of Pittsburgh, Pittsburgh, PA) and rat ASIC2a (rASIC2a) in the pRSSP6009 vector (provided by Stefan Gründer, RWTH Aachen University, Aachen, Germany), respectively. Mutant cDNAs were generated with custom oligomers (Eurofins Genomics) and Pfu Ultra II Fusion HS DNA Polymerase (Agilent Technologies), following suppliers' PCR protocols, and sequences of the full ASIC inserts

Figure 1. **ASIC membrane-spanning region. (A)** Left, MD simulation system for rASIC2a model based on PDB accession no. 4NTW (each subunit a different color) embedded in a lipid bilayer (cyan) in NaCl solution (water, red and white sticks; Na$^+$ and Cl$^-$, orange and cyan balls). Right, magnified view of M1 and M2 from a single subunit, showing residues discussed in main text. Residues G10′, A11′, S12′, shown in single letter code. **(B)** M1 and M2 segments from an amino acid sequence alignment of chick ASIC1 (cASIC1), mouse ASIC1a (mASIC1a), and rat ASIC2a (rASIC2a). (The chick *ASIC1* gene does not undergo splicing like mammalian *ASIC1*, hence the single cASIC1 product.) mASIC1a amino acid sequence is 89% and 98% identical to cASIC1 and human ASIC1a, respectively. rASIC2a is 64% and 99% identical to cASIC1 and human ASIC2a, respectively.

were confirmed (GATC Biotech). Plasmids were linearized with EcoRI (mASIC1a) or NaeI (rASIC2a), and complementary RNAs (cRNAs) were transcribed with the Ambion mMESSAGE mMACHINE RNA transcription kit (Thermo Fisher Scientific). Stage V or VI *Xenopus laevis* oocytes were isolated and maintained as described previously (Lynagh et al., 2017b). Oocytes were injected with 0.8 ng cRNA, unless currents were undetectable, in which case 40 ng was also injected and tested (e.g., Fig. 4 B).

After 24–48 h, oocytes were placed in a custom-built recording chamber (Dahan et al., 2004) and continuously perfused with bath solution containing (in mM) 96 NaCl, 2 KCl, 1.8 CaCl$_2$, and either 5 HEPES (pH > 5.5) or 5 2-(N-morpholino)ethanesulfonic acid (pH ≤ 5.5). Control (pH 7.5) and low pH solutions were exchanged with a ValveBank 8 perfusion system (AutoMate Scientific). Oocytes were two-electrode voltage-clamped with an OC-725C amplifier (Warner Instruments) and Digidata 1550 digitizer (Molecular Devices). In establishing proton

sensitivity, half-maximal effective proton concentrations (pH_{50}) were established in concentration–response experiments, where decreasing pH solutions were applied to oocytes between resting periods of ~1 min, performed at –40 mV. In experiments to establish relative permeability (e.g., P_{Na^+}/P_{K^+}), the holding potential was clamped at –80 mV, and 200-ms voltage ramps were applied from –80 to +60 mV during activation by saturating proton concentration (pH 6.0 for most ASIC1a homomers, pH 5.0 for most heteromeric channels, and pH 3.5 or 4.0 for ASIC2a homomers). Currents during the same voltage ramps at pH 7.4 were subtracted from currents during activating pH (Fig. 2 A) in measuring reversal potentials of proton-gated currents (V_{rev,Na^+}) in regular (96 mM NaCl) or LiCl-, KCl-, or CsCl-substituted bath solution. Relative permeability was calculated with the Goldman–Hodgkin–Katz equation, $P_{K^+}/P_{Na^+} = \exp[F(V_{rev,Na^+} - V_{rev,K^+})/RT]$, where F = Faraday's constant, R = gas constant, and T = 294K.

Each construct was expressed and recorded in at least two batches of oocytes. All data analysis was performed in GraphPad Prism 7. pH_{50} values were calculated from individual experiments using the Hill equation (four parameters, variable slope), and mean ± SEM is reported in the main text and in graphs of pH_{50} values. Curves in figures, for illustration, are fits to averaged data points (mean ± SEM). As discussed in the main text (see Fig. 4 A), WT ASIC1a/ASIC2a heteromer concentration–response data could be fitted with a biphasic curve, due to a small population of ASIC1a homomeric channels. This was not the case for mutant-containing heteromers, where presumably, mutant homomers showed decreased channel function or expression compared with WT homomers. Where appropriate, mutant pH_{50} values were compared with WT with one-way analysis of variance and compared with WT with Dunnett's multiple comparison test. In reporting relative permeability ratios (e.g., P_{Na^+}/P_{K^+}), mean ± SEM is shown on a log scale for clarity. Whereas certain mutations clearly reduced P_{Na^+}/P_{K^+} from ~6 at WT channels to unity, mutants with "intermediate" values rarely differed significantly from WT, likely due to the reasonably low level of Na$^+$/K$^+$ selectivity in ASIC. Small decreases in relative permeability should therefore be interpreted with some caution.

MD simulations

As there are currently no high-resolution structures of ASIC2a or ASIC1a/ASIC2a channels available, models of rASIC2a, mASIC1a/mASIC1a/rASIC2a, and mASIC1a/rASIC2a/rASIC2a were created based on the cASIC1 channel PDB accession no. 4NTW (Baconguis et al., 2014; available residues 45–456; PDB numbering). The side chains of the amino acids in the cASIC1 structure were manually mutated to the corresponding residues in the mASIC1a or rASIC2a sequence (Figs. 1 B and S1 B). Each protein was embedded in a hydrated lipid bilayer of 386 (194 top and 192 bottom) palmitoyl-oleoyl-phosphatidylcholine lipids, with 47,184 water molecules and 150 mM of NaCl or KCl (162 Na$^+$ or K$^+$, and 109 Cl$^-$ ions), to form 115 × 115 × 160-Å periodic simulation boxes containing 212,977 atoms (Fig. 1 A).

Systems were built and equilibrated with the CHARMM program (Brooks et al., 1983, 2009), using the C36 lipid (Klauda et al., 2010) and CHARMM22 protein parameters (MacKerell

et al., 1998) with CMAP corrections (Mackerell et al., 2004) and TIP3P water (Jorgensen et al., 1983). Ion parameters used were those for the CHARMM27 forcefield, with revisions to Na$^+$ and K$^+$ nonbonded Lennard–Jones (LJ; referred to as CHARMM27*), corresponding to r_{min} values for ion-carboxylate oxygen pair interactions of 3.12 and 3.46 Å, respectively (Noskov and Roux, 2008). We have previously demonstrated that these parameters yield agreement with experimental and quantum mechanical measures of binding of Na$^+$ to carboxylates in aqueous solution (Lynagh et al., 2017a), comparable to alternative parameters designed to fit experimental osmotic pressure coefficients (Marinelli et al., 2014). While the precise ion-carboxylate LJ parameter will affect ion free energies within the ASIC pores, we have previously shown that selective binding is maintained regardless of the choice (Lynagh et al., 2017a). Modified LJ parameters, however, were used to describe the interactions between cations and carbonyl oxygen atoms of the protein to reproduce free energies of solvation in protein backbone mimetic, N-methyl-acetamide (Bernèche and Roux, 2001; Noskov et al., 2004; Allen et al., 2006; Flood, 2019).

After a total of 3,000 steps of steepest descent and adopted basis Newton–Raphson energy minimization, MD simulations commenced with initial harmonic restraints (10 kcal/mol/Å^2) applied to all heavy atoms. These restraints were slowly released over 0.5 ns, followed by 1.5 ns of initial equilibration without any restraints. Equilibration simulations were run initially with constant volume using a timestep of 1 fs for 50 ps, before switching to constant pressure (1 atm) with a timestep of 2 fs. Production simulations used NAMD v2.9 (Phillips et al., 2005) with the same forcefield. Simulations were performed using tetragonal periodic boundary conditions at constant pressure (1 atm) with a Langevin piston (Andersen, 1980; Feller et al., 1995) and constant temperature (303°K; above the gel phase transition temperature of 271°K) using a Nosé-Hoover thermostat (Hoover, 1985; Nosé, 1984). All bonds to H atoms were maintained using SHAKE (Ryckaert et al., 1977) in CHARMM and RATTLE (Andersen, 1983) in NAMD. Electrostatic interactions were computed using the particle mesh Ewald method, with grid spacing of 1.5 Å and sixth order B-spline for mesh interpolation. Nonbonded pair lists were updated every 20 fs in NAMD (and heuristically in CHARMM) with a neighbor list distance of 16 Å and a real space cutoff of 12 Å, with energy switch distance of 10 Å.

Model structures were subjected to initial unbiased MD simulations to relax structures and examine ion binding. This included ~180-ns simulations for rASIC2a and ~200-ns simulations for mASIC1a/mASIC1a/rASIC2a and mASIC1a/rASIC2a/rASIC2a heteromeric channels in both NaCl and KCl solutions. To examine protein stability, we calculated RMSD values for transmembrane 1 (TM1) and TM2 helices, as well as separate RMSD calculations for residues 60–75 in TM1 and –7′ to 21′ in TM2, excluding residues at the termini of the truncated sequence of PDB accession no. 4NTW, to isolate changes in the lower M1 and M2 helix. The overall shape of the rASIC2a model remains consistent with the cASIC1 structure (PDB accession no. 4NTW; Fig. S2), where we see that all six simulations led to close alignment after 100 ns, with only small deviations in the lower

TM helices. We observed dynamic behavior of the residues at the intracellular end of the M2 helix (in particular I22′ and Y23′), expected given the absence of intracellular N- and C-termini that were not resolved in the PDB accession no. 4NTW structure. As the channels relaxed, we observed increases in RMSD values to 2–2.5 Å for TM1 and TM2 (Fig. S3; orange), but limited to 1–1.5 Å when excluding the residues at the intracellular side of the helices (Fig. S3; blue) within the first ~100 ns. In some simulations, we observed late changes by an additional ~0.5 Å due to termination of the sequence and solvent exposure. These changes are associated with slight splaying of the lower M1 helix as well as unfolding and refolding of residues I23′ and Y22′ at the intracellular end of the M2 helices (compare red and blue lines in Fig. S3) and are more prevalent in rASIC2a-containing models, possibly a result of the more hydrophobic rASIC2a I23′ residue (A23′ in cASIC1 or mASIC1a) that is exposed to solvent, preferring to be directed toward lipids (see Fig. S4 C). This dynamics of the lower M1 and M2 helices is considered to be an unavoidable consequence of the PDB accession no. 4NTW structural template, lacking N- and C-termini, and to have minimal bearing on the ion energetics throughout the channel.

Estimates of the free energy profiles for ion translocation across the channel pores (Fig. S5) were calculated as $W(z) = -k_B T\ln[\rho(z)] + C$, where ρ is the unbiased probability distribution as a function of reaction coordinate z, being the position of the ions along the z axis relative to the GAS sequence center of mass, with constant C chosen to set the zero of the free energy in bulk electrolyte. The mean and SEM were obtained by dividing data into four equal blocks for each simulation. However, to ensure thorough sampling of free energies for individual Na$^+$ or K$^+$ ions translocating the pore, we performed umbrella sampling (US; Torrie and Valleau, 1977) simulations, using the relaxed models. This involved 49 independent simulations (windows) with 1-Å spacing: windows spanning –25 to 23 Å, relative to the GAS center of mass. Initial configurations were taken from the unbiased simulations after equilibration for 100 ns. In each window, the ion was held near the window central position by a 2.5 kcal/mol/Å^2 force constant, chosen because it corresponds to a positional standard deviation of ~0.5 Å, according to equipartition theorem at 303K, ensuring overlapping distributions for neighboring windows. To increase sampling efficiency, the radial position of the ion was constrained with a flat bottom potential to keep it in a cylinder of 9 Å with a force constant 10 kcal/mol/Å^2. This radius was chosen as it was the minimal radius that allows the ion to explore all residues of interest in the pore. We ran 20 ns per window, with an additional 7 ns in windows between –10 and –5 Å and between 15 and 20 Å to achieve convergence in wider regions of the pore containing several charged residues (Fig. S6). The first 8/11 ns for rASIC2a, 12/6 ns for mASIC1a/mASIC1a/rASIC2a, and 6/5 ns for mASIC1a/rASIC2a/rASIC2a heteromeric channels were discarded as equilibration for Na$^+$/K$^+$. Free energy profiles were then calculated using the Weighted Histogram Analysis Method (Kumar et al., 1992). Mean and SEM were calculated by dividing the data into 1-ns blocks. Due to the wide nature of the pore at the extracellular side and binding to the charged glutamate

(positions 59 and 62 in rASIC2a and position 63 in mASIC1a) and aspartate (position 0′ in mASIC1a and rASIC2a) residues, we experienced lack of convergence in the US simulations in this region (Fig. S6). To overcome this, we combined the results from the unbiased simulations, which achieved similar free energy profiles within the channels (see Fig. S6), as well as good sampling of ions in the vestibular regions. This was done by removing the umbrella windows above z = 11 Å and incorporating the unbiased trajectory into the weighted histogram analysis method solution to produce the final profiles shown in Figs. 3 and 5.

The protein/water coordination of the Na$^+$ and K$^+$ ions during permeation of the pore was determined by counting the number of oxygen atoms from water and protein in the first solvation shell of the ions. The solvation shell was defined based on the first minimum in the radial distribution functions for Na$^+$ and K$^+$ ions in bulk solution, far from the protein (3.2 and 3.8 Å, respectively). The total coordination number was expressed relative to bulk values (5.67 ± 0.04 and 6.94 ± 0.07 water molecules for Na$^+$ and K$^+$; also obtained from analysis of bulk radial distribution functions).

The influence of the electrostatic potential arising from residues E59 and E62 in rASIC2a, and V61 and N64 in cASIC1, was estimated by solving the linearized Poisson–Boltzmann equation using the PBEQ module in CHARMM (Im et al., 1998; Nina et al., 1997). To isolate these residues, the charges of all other atoms were set to zero. A grid of 601 × 601 × 601 points with cell spacing 1.0 Å was used and focused to 301 × 301 × 301 points with cell spacing 0.5 Å with periodic boundary conditions in the x and y directions. Protein, membrane, and water dielectric constants ($\varepsilon_{protein} = \varepsilon_{membrane} = 2$, $\varepsilon_{water} = 80$) were assigned, with the channel pore assigned bulk water dielectric based on any grid points within a cylindrical region of radius 10 Å not overlapping with the protein, allowing for the vestibules of the TM pore. Dielectric assignments were performed using a reentrant probe method, as described by Allen et al. (2004). The concentration of NaCl solution in bulk was set to 150 mM, but to zero inside the cylinder to avoid artificial Debye screening in the pore.

Online supplemental material

Fig. S1 shows differences in the structures of cASIC1 and rASIC2a. Fig. S2 shows structural alignments of M2 helices between cASIC1 homomer crystal structure and mASIC1a/mASIC1a/rASIC2a heteromer, mASIC1a/rASIC2a/rASIC2a heteromer, and rASIC2a homomer models after 100 ns simulation. Fig. S3 shows RMSD for the backbone of TM1 and TM2 in simulations. Fig. S4 shows behavior of the lower pore of cASIC1 and rASIC2a in simulations. Fig. S5 shows potentials of mean force for Na$^+$ and K$^+$ in heteromers and homomeric rASIC2a. Fig. S6 shows convergence of potentials of mean force from Umbrella Sampling simulation. Fig. S7 shows behavior of the upper pore of cASIC1 and rASIC2a in simulations. Fig. S8 shows Na$^+$ and K$^+$ first shell coordination by oxygen atoms from water and protein. Fig. S9 shows lack of functional expression in oocytes when replacing A11′ with lactic acid ("α") in rASIC2a channels. Fig. S10 shows comparison of the potentials of mean force for cASIC1, rASIC2a, and mASIC1a/rASIC2a heteromers.
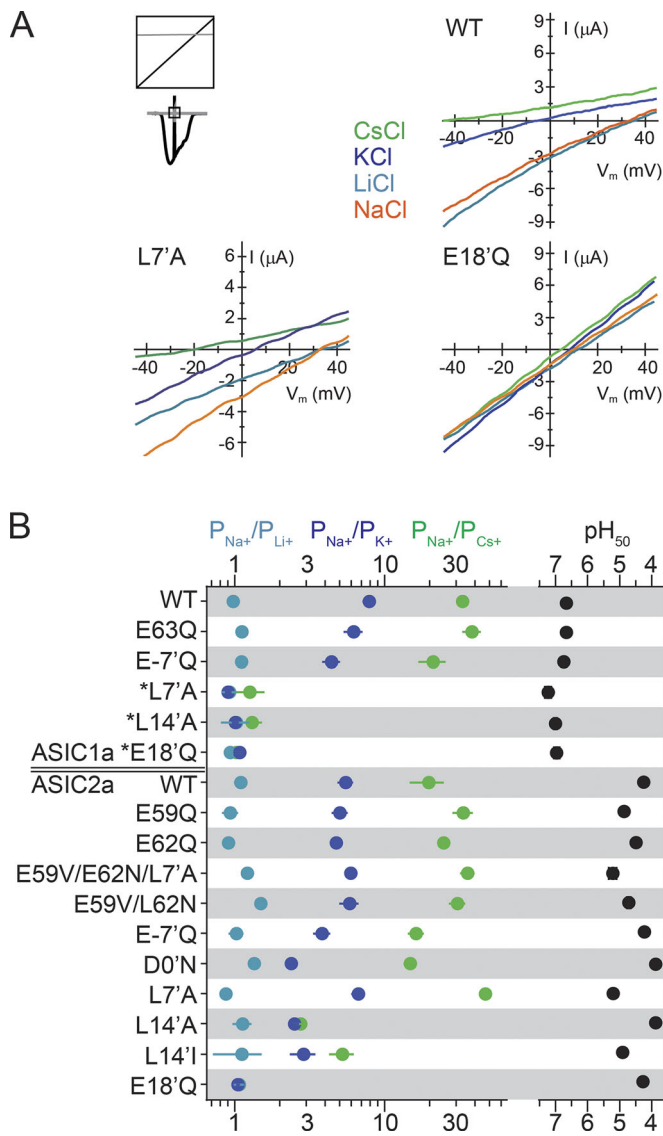
Lynagh et al.
Ion selectivity in ASIC heteromers

Journal of General Physiology   4 of 12
https://doi.org/10.1085/jgp.201812297

Figure 2. **Site-directed mutagenesis and relative ion permeability of homomeric ASIC1a and ASIC2a.** **(A)** Protocol and example recordings of current–voltage (I-V) relationship for WT rASIC2a and indicated mutants, assayed by proton-gated current during $-80 \rightarrow 60$ mV ramp; current during voltage ramp in resting pH (gray) was subtracted from current during voltage ramp at activating pH (3.5–4.0, black), giving the currents in the I-V plots, as indicated in top left panel. **(B)** Relative permeability ratios (P_{Na^+}/P_{X^+}) and half-maximal pH for activation (pH_{50}) for WT and mutant mASIC1a and rASIC2a homomeric channels (mean ± SEM). *, data from Lynagh et al. (2017a).

Results

Effects of M2 mutations on homomeric ASIC2a ion selectivity

We began our investigation into the determinants of ion selectivity in ASIC2a-containing channels by measuring relative ion permeability (P_{Na^+}/P_{X^+}) through homomeric channels. In the absence of knowledge on determinants of selectivity in ASIC2a, we generated rat ASIC2a (rASIC2a) channels carrying mutations equivalent to those that affected ion selectivity or conduction (D0′N, L7′A, L14′A, E18′Q) or abolished detectable channel function (G10′A, S12′A) in mouse ASIC1a (mASIC1a; Fig. 1 A illustrates the location of these residues). In homomeric rASIC2a

channels, the E18′Q mutation reduced P_{Na^+}/P_{K^+} from 5.5 ± 0.6 at WT ($n = 5$) to unity (Fig. 2, A and B), and G10′A and S12′A mutations abolished detectable channel activity (see also Fig. 4 B). The results closely reflect those obtained with mASIC1a, where E18′ mutations abolish selectivity, but where conventional mutagenesis on the GAS residues renders channels nonfunctional and thus fails to shed light on their roles (Lynagh et al., 2017a). Although the rASIC2a D0′ mutation caused a subtle reduction in P_{Na^+}/P_{K^+} (2.4 ± 0.1, $n = 8$), it did not alter the overall relative permeability profile (Fig. 2 B), somewhat reminiscent of the subtle effects of the D0′N mutation in human ASIC1a channels (Yang and Palmer, 2014). ASIC2a L14′A and L14′I mutations also reduced selectivity, but less so than the E18′Q mutation ($P_{Na^+}/P_{K^+} = 2.5 ± 0.2$, $n = 5$; $P_{Na^+}/P_{K^+} = 3.0 ± 0.5$, $n = 4$), again reflecting results in mASIC1a, although the difference between alanine and isoleucine substitutions was more marked in mASIC1a (L14′A $P_{Na^+}/P_{K^+} = 1.00 ± 0.05$, $n = 6$, and L14′I $P_{Na^+}/P_{K^+} = 5.8 ± 1.0$, $n = 5$, from Lynagh et al. [2017a]). rASIC2a L7′A channels, however, showed ion selectivity similar to or possibly slightly increased over that of WT (Fig. 2, A and B; P_{Na^+}/P_{K^+} 6.7 ± 0.7, $n = 5$; WT: P_{Na^+}/P_{K^+} 5.5 ± 0.6, $n = 5$), which is in stark contrast to homomeric mASIC1a L7′A channels, which are nonselective (P_{Na^+}/P_{K^+} 1.0 ± 0.1, $n = 5$, from Lynagh et al. [2017a]). This implies that L7′ may play a bigger role in ion selectivity in ASIC1a than in ASIC2a. However, we acknowledge that while the observed reversal potentials were relatively consistent across experiments, the slopes for the different ions were variable, likely due to small differences in pH and timing of the voltage ramp.

We also tested rASIC2a mutants for potency of activation by protons. L7′A and L14′I mutations caused substantial increases in proton potency (WT $pH_{50} = 4.3 ± 0.2$, $n = 5$; L7′A $pH_{50} = 5.2 ± 0.1$, $n = 5$; L14′I $pH_{50} = 4.9 ± 0.1$, $n = 4$, both mutants $P < 0.001$ compared with WT), whereas L14′A ($pH_{50} = 3.9 ± 0.2$, $n = 4$) and other M2 mutations had relatively modest effects (Fig. 2 B). This loosely reflects results with mASIC1a, where L7′ and L14′ mutations increased proton potency (Lynagh et al., 2017a). Together, these results tentatively suggest that in terms of channel gating, conserved residues play similar roles in ASIC1a and ASIC2a homomers (although nonconserved side chains, such as the ASIC2a-specific E59, can also have significant effects on gating: E59Q $pH_{50} = 4.9 ± 0.1$, $n = 5$; E59Q/L7′A $pH_{50} = 5.7 ± 0.1$, $n = 5$). In terms of ion selectivity, the role of some residues is conserved: D0′ in the upper pore and E18′ in the lower pore play modest and strong roles, respectively, in ion selectivity in ASIC1a and ASIC2a. However, near the GAS belt in the middle of the pore, L14′ contributes similarly to ion selectivity in both subtypes, whereas L7′ is crucial for selectivity in ASIC1a, but not in ASIC2a. The role of the GAS belt itself remains to be elucidated for ASIC2a, although G10′ and S12′ are clearly important for the expression of functional channels.

MD simulations identify differences in ion permeation in ASIC1a and ASIC2a homomeric channels

To explore the role of the GAS belt and potentially explain the different role of L7′ in rASIC2a, we performed MD simulations to compute the potential of mean force (PMF) describing

Lynagh et al.
Ion selectivity in ASIC heteromers

Journal of General Physiology
https://doi.org/10.1085/jgp.201812297

5 of 12

permeation of Na⁺ and K⁺ ions through a model of rASIC2a based on the open-channel cASIC1 structure (PDB accession no. 4NTW), shown in Fig. 3 A. Overall, the PMFs for Na⁺ and K⁺ permeating the rASIC2a model (Fig. 3 A; solid lines) show broadly similar shapes to those found for the cASIC1 structure (Fig. 3 A; dashed line, from Lynagh et al. [2017a]), with a well at the bottom of the pore (at z = –8.2 and –8.9 Å, for Na⁺ and K⁺, respectively) and a barrier around GAS (at z = –0.5 Å), but with a distinct well for both ions in the upper pore of rASIC2a (at z = 14.7 and 15.7 Å, for Na⁺ and K⁺, respectively) that was not present in cASIC1. At the bottom of the rASIC2a pore, we see an energetic preference for Na⁺ over K⁺ of ~1.5 kcal/mol around E18′, suggestive of a selective binding site (Fig. 3 A). This is consistent with the loss of selectivity in E18′Q rASIC2a mutant channels, in which the negative charge of E18′ is removed, and with our previous observations of preference for Na⁺ at E18′ in cASIC1 (dashed curves in Fig. 3 A).

The differences between the Na⁺ free energy minima seen for cASIC1 and rASIC2a around E18′ and D21′ are interesting, but are small (only 0.2 kcal/mol). However, there is a change in the shape of that minimum, where it appears to be more localized around E18′ in rASIC2a. This is due to a stronger reliance on E18′ coordination, with less involvement of D21′, as shown in Fig. S4 (A and B), where we see a reduction in multi-ion complexes. We explain this from the movement of the D21′ away from E18′, due to interactions with the M2 terminus, and interactions of the neighboring hydrophobic I23′ at the lipid interface (Fig. S4 C).

In the upper half of the rASIC2a pore, we see wells both for Na⁺ and K⁺ ions around the level of M1 E59 and E62 and M2 D0′ (Fig. 3 A, solid curves at z = 14 Å). This well is unique to rASIC2a and attributed to the electrostatic fields originating from the charged E59 and E62 side chains that are only present in rASIC2a (Fig. 1 B). Fig. S7 describes the binding of one to two ions to each subunit at this location, where we see off-axis binding sites (on average ~13.6 ± 0.2 Å from the channel axis), directed to the side (Fig. S7 B). Figs. 3 B and S7 C show the electrostatic potential due to these M1 residues alone, from solution to the Poisson–Boltzmann equation (that includes ionic screening due to counterion binding to these carboxylate-lined sites; see Materials and methods). The strong electric fields lead to an expansive attractive region for cations that can explain the origin of this unique feature in the rASIC2a PMFs. This feature also exhibits an energetic preference for Na⁺ over K⁺ by ~1 kcal/mol (compare in Fig. 3 A), owing to stronger binding of the smaller ion to high-field-strength carboxylate groups (Roux, 2010), as evidenced by the significantly larger peak in protein coordination for Na⁺ in Fig. S8 C, compared with K⁺. However, as E59 and E62 carboxylates reside away from the channel axis, their main role may be to create a long-ranged attraction that may not affect permeation selectively. Consistent with this interpretation, we saw no change in ion selectivity when we measured relative ion permeability in either rASIC2a channels containing the E59Q and E62Q mutations (aimed at decreasing this negative electrostatic potential) or rASIC2a channels containing the E59V/E62N double mutation (aimed at removing all of this negative electrostatic potential and mimicking the cASIC1 residues; Fig. 2 B). Similarly, we saw no decrease in ion selectivity in E63Q mASIC1a

channels (Fig. 2 B). Further toward the extracellular side of the pore, another glutamate residue at position –7′ in M2 corresponds to a position with slight energetic preference for Na⁺ in the PMF profile for rASIC2a (Fig. 3 A). However, as E-7′ is located far from the z axis and points away from the pore, it is also unlikely to affect selectivity, as reflected in our experiments, where the E-7′Q mutation had little effect on ion selectivity in either rASIC2a or mASIC1a channels (Fig. 2 B).

The free energy increases rapidly from the minima in the lower pore around E18′ to a peak around the GAS belt (Fig. 3 A, solid curves). Above the GAS belt, around the L7′ residue, the free energy falls by 2.3 and 1.9 kcal/mol for Na⁺ and K⁺, respectively. This contrasts with the cASIC1 simulations, in which the barrier was higher adjacent to the L7′ site than for the crossing of the GAS constriction for K⁺ (dashed blue curve in Fig. 3 A) and was thus expected to control conduction for that ion. Instead, in rASIC2a, the attractive fields from the upper charges generate a gradient that lowers the free energy of the ions near L7′ so that it is no longer the maximum for K⁺ (solid blue curve in Fig. 3 A). This significant downhill slope is well captured by the 1D profiles of electrostatic potential due to those residues, shown in Fig. 3 B (left). The possibility of L7′ having decreased influence on conduction, apparently no longer being rate limiting, is a likely contributor to the absence of effect of the L7′A mutation on ion selectivity in rASIC2a (Fig. 2 B). This is in contrast to cASIC1, which experienced a complete loss of selectivity for the L7′A mutant. It may also increase the influence of the GAS belt in rASIC2a, which is now the highest point for both Na⁺ and K⁺ ions, with similar free energy relative to bulk solution. We note, however, that the correspondence between local thermodynamic stabilities of different ions and the relative permeabilities for the channel must ultimately be determined by conduction kinetics for each ion, as witnessed, for instance, in studies of potassium channels, where selectivity can be influenced by changes in ion interactions in disparate locations (e.g., Grabe et al. [2006]).

We thus considered that, in the absence of the upper negative charges, the L7′A mutation might begin to influence ion selectivity in rASIC2a. Surprisingly, however, E59V/E62N/L7′A triple mutant rASIC2a channels showed little change from E59V/E62N or WT ion selectivity (P_{Na^+}/P_{K^+} remains around 6; Fig. 2 B). By eliminating E59 and E62 charges in rASIC2a, mimicking the cASIC1 channel, L7′ had the potential to become rate determining for K⁺ ions. That the experiments for the E59V/E62N rASIC2 double mutant did not reveal a reinstating of a role for L7′ in selectivity suggests that other differences, such as pore size, or ion interactions in the vicinity of L7′ might also contribute to reduced involvement of L7′. We note that the pore radius profiles for cASIC1 and rASIC2a are similar, but with a small increase in ASIC2a throughout the upper pore (by 0.3 ± 0.2 Å around L7′; Fig. S1 A). This could be caused by sequence differences (primarily on the lipid-facing side of the M1 helices) that may affect relative helix interactions, as illustrated in Fig. S1 B. This would help reduce ion hydration losses and lower free energies in the upper pore (Fig. 3 A), in addition to the effects of the long-ranged E59/E62 interactions. Alternatively, lack of effect of L7′ may be due to local differences for K⁺ and Na⁺ around L7′ itself. We note that the WT cASIC1 channel exhibited a peak
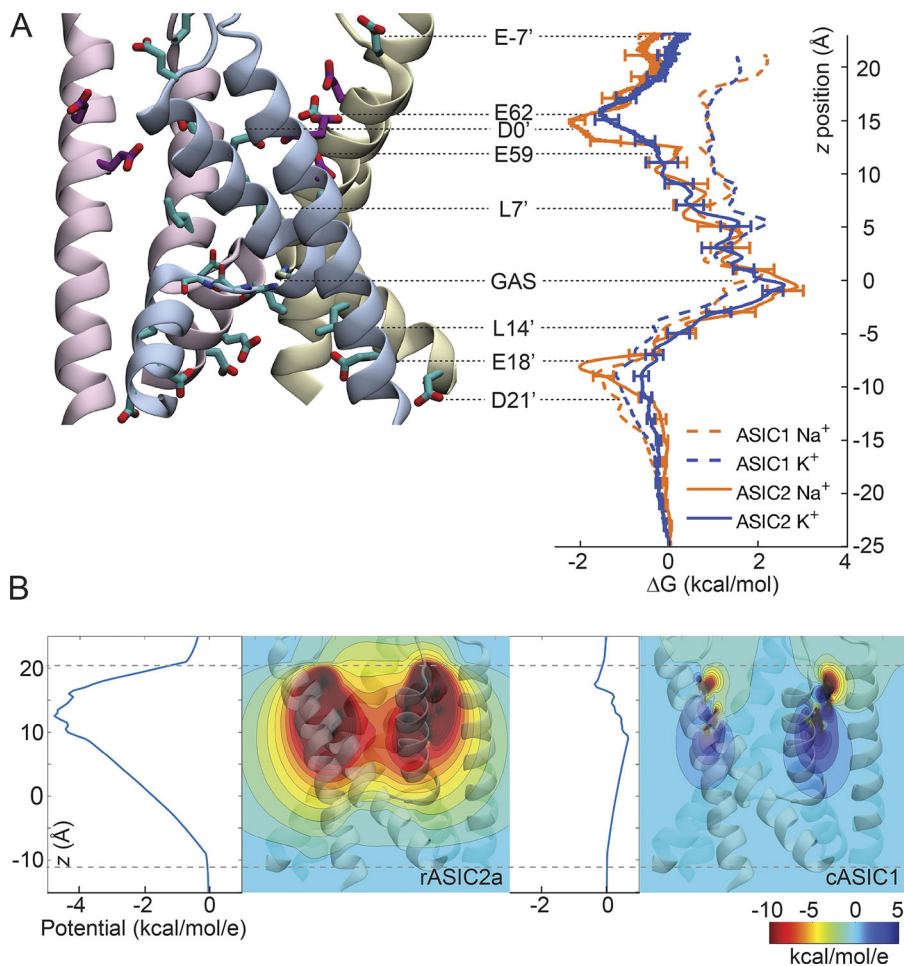
Figure 3. rASIC2a MD free energy simulations. (A) Single ion free energy profiles for Na$^+$ (orange) and K$^+$ (blue) through the pore of cASIC1 (data from rASIC2a model and Lynagh et al. [2017a] shown as solid and dotted lines, respectively), with error bars represented by ±1 SEM. Inset shows corresponding residues in cyan with E59 and E62 in rASIC2a and V61 and N64 in cASIC1 highlighted in purple. **(B)** Electrostatic potential from E59 and E62 in rASIC2a and V61 and N64 in cASIC1. The dotted lines indicate the position of the membrane.

barrier for K$^+$ at L7′ (potentially rate determining) that was not present for Na$^+$, leading to a maximum difference in free energy between Na$^+$ and K$^+$ ions near the L7′ site of 1.3 ± 0.2 kcal/mol. This was a result of more substantial partial K$^+$ dehydration, not compensated for by protein coordination (loss of 0.31 ± 0.03 and 0.82 ± 0.04 water molecules, and 0.31 ± 0.03 and 0.86 ± 0.04 total oxygen coordination for Na$^+$ and K$^+$, respectively) in this narrow part of the pore (Lynagh et al., 2017a). In WT rASIC2a we see a reduced difference in free energy near this site (at maximum 0.7 ± 0.4 kcal/mol; Fig. 2 A), which may be attributed in part to slightly smaller hydration losses (by 0.15 ± 0.02 and 0.72 ± 0.02 for Na$^+$ and K$^+$, respectively; again with essentially no protein oxygen coordination) in rASIC2a (Fig. S8). This is likely due to overall widening of the upper pore (Fig. S1 A), because the L7′ side chains themselves are positioned between TM helices, thus not directly affecting pore radius. These side chains have, however, moved 0.4 ± 0.1 Å closer to the channel axis (with essentially zero movement of their backbones) and are similarly or slightly more flexible in the rASIC2a channel (RMSD of 1.22 ± 0.04 Å in rASIC2a vs. 1.13 ± 0.03 Å in cASIC1). Although these changes are marginal, in conjunction with the increase in pore radius to improve ion hydration, they may explain the reduced impact of L7′ mutation on selectivity in rASIC2.

Analysis of ion solvation around the GAS belt shows the protein compensating for partial K$^+$ desolvation (similar to that seen

in cASIC1; Lynagh et al., 2017a), which explains the lack of free energy difference between Na$^+$ and K$^+$ at the GAS belt (Fig. S8, C and D). The greatest constriction in the GAS belt is formed by main chain oxygen atoms from G10′ residues (Baconguis et al., 2014). Seeking experimental verification of a contribution of G10′ to ion selectivity in rASIC2a channels, we attempted to express mutant rASIC2a channels containing an ester carbonyl rather the canonical amide carbonyl between G10′ and A11′ (Fig. S9). To this end, we replaced A11′ with lactic acid (α), which reduces electron density around the G10′ carbonyl oxygen via the main chain ester bond, which previously revealed contributions of G10′ in mASIC1a channels (Lynagh et al., 2017a). However, rASIC2a channels failed to incorporate α or were entirely nonfunctional, thus preventing us from dissecting the role of the backbone carbonyl in selectivity (Fig. S9). Regardless, our results suggest that GAS exhibits the largest barrier to cross for ion conduction in rASIC2a, and is thus expected to control the rate of permeation for both ionic species. Although our analysis does not reveal a difference in stability of the ions in the GAS constriction in the WT channels, potentially, if this site were to be modified in a way that altered the energetics of Na$^+$ and K$^+$ differently, we suggest that the GAS belt would be more likely to affect channel selectivity in ASIC2a than in ASIC1a. Ultimately, very long (millisecond-order) MD simulations under the action of membrane potentials could be used to observe the rate-limiting processes for Na$^+$ and K$^+$
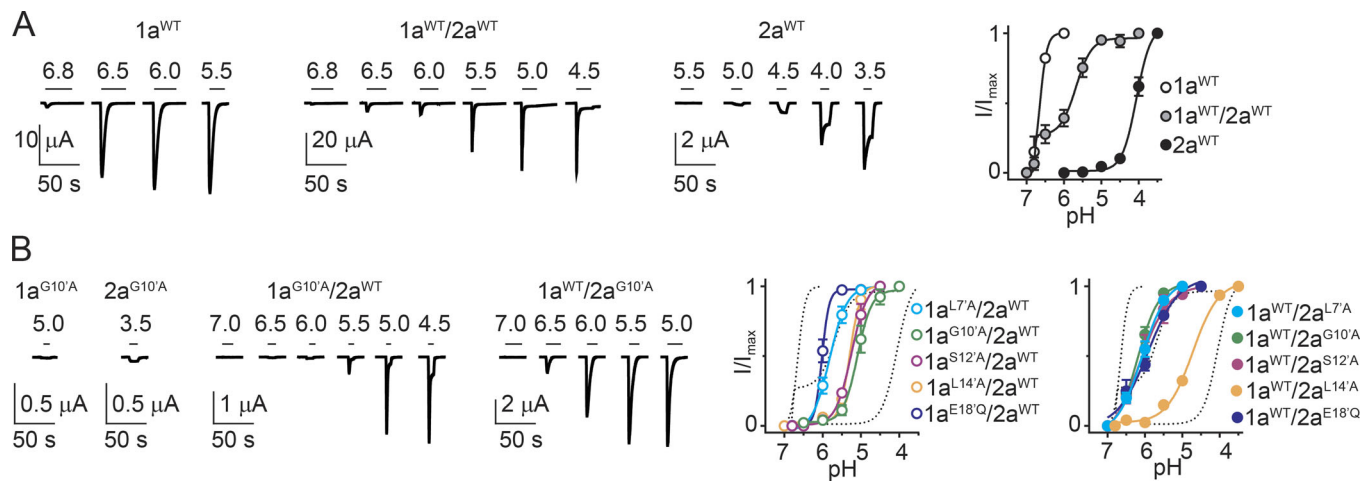
Figure 4. **Expression mASIC1a/rASIC2a heteromers. (A)** Example current responses (left) to decreasing pH in oocytes injected with cRNAs for mASIC1a; mASIC1a and rASIC2a (in a 1:1 ratio); or rASIC2a and averaged (±SEM), normalized peak current responses to decreasing pH (right panel, n = 4–6). $1a^{WT}/2a^{WT}$ is fitted with a biphasic curve. **(B)** Example current responses (left) to decreasing pH in oocytes injected with mutant cRNA, alone or in combination with WT cRNA of the other isoform and averaged (±SEM), normalized peak current responses to decreasing pH (right, n = 3–5). WT curves from A are shown as dashed lines for comparison.

permeation and to capture the effects of mutations on ion selectivity in each member of the ASIC family.

When studying the PMF around L14′ (z ≈ −5 Å in Fig. 3 A), we observed no energetic preference for Na^+. This seems inconsistent with results from mutagenesis experiments, which showed moderately decreased Na^+ selectivity in channels with L14′A and L14′I mutations (Fig. 2 B). We had previously argued (Lynagh et al., 2017a) that this could be attributed to artificial splaying of the lower pore of the PDB accession no. 4NTW structure, as a result of the truncation of substantial portions of the intracellular N- and C-termini of cASIC1 (Baconguis et al., 2014). In support of this notion, we showed that ASIC1a simulations based on a narrower lower pore (PDB accession no. 2QTS) lead to Na^+ multi-ion/multicarboxylate complexes with E18′ and D21′ that could promote conduction of Na^+ ions (Lynagh et al., 2017a). Arguing against our suggestion that a full-length ASIC structure might adopt a much tighter lower pore, a recent cryo-EM structure with full-length cASIC1 (in the resting state; PDB accession no. 6AVE) show a similarly splayed lower pore compared to the truncated structures (Yoder et al., 2018). The pore diameter around E18′ in PDB accession no. 6AVE is, however, ∼1 Å narrower than in the corresponding truncated x-ray structure (PDB accession no. 5WKV) from the same study. Second, and perhaps more likely, L14′ side chains are oriented toward adjacent helices and may contribute to ion selectivity by shaping the lower pore and influencing the roles of, for example, E18′ and D21′ side chains. Indeed, L14′ mutations affect channel gating, as interpreted from altered pH_{50} values (Fig. 2 B), further indicative of L14′ side chains affecting conformational changes in the channel (Lynagh et al., 2017a).

Effects of M2 mutations in heteromeric ASIC1a/ASIC2a channels

As GAS belt mutations, conventional or otherwise, failed to generate ASIC2a channels with measurable currents, we lack an experimental test of the role of the GAS belt in ion selectivity of

ASIC2a-containing channels. We therefore turned to heteromeric ASIC1a/ASIC2a channels, considering that heteromers assembled by WT ASIC1a and mutated ASIC2a subunits could be more functional than mutant ASIC2a homomers. Furthermore, little is known about ion selectivity in heteromeric channels. We therefore tested the effects of certain M2 mutations on ion selectivity in mASIC1a/rASIC2a heteromers. The expression of such channels is possible through the coinjection of oocytes with ASIC1a and ASIC2a cRNAs, whereby a 1:1 ratio of cRNAs yields mostly heteromeric channels (>80%) and a smaller population of homomeric channels (Bartoi et al., 2014; Bassilana et al., 1997). Our proton concentration–response experiments confirmed the robust expression of heteromeric channels. In mASIC1a-injected oocytes, maximum current responses were activated around pH 6.0 (pH_{50} = 6.66 ± 0.03, n = 4; Fig. 4 A), and in rASIC2a-injected oocytes, large currents were not activated by pH > 4.5 (pH_{50} = 4.3 ± 0.2, n = 5; Fig. 4 A), consistent with previous studies of homomeric channels (Kellenberger and Schild, 2015). In contrast, in 1:1 mASIC1a:rASIC2a-injected oocytes, maximum current amplitude was activated around pH 5.0 ($pH_{50,B}$ = 5.6 ± 0.2, n = 6), indicative of a predominant population of heteromeric channels (hereafter $1a^{WT}/2a^{WT}$), despite a smaller population of mASIC1a homomers evident in the first phase of the biphasic concentration–response curve in Fig. 4 A ($pH_{50,A}$ = 6.6 ± 0.1, n = 4; the first phase was less prominent in some recordings). Overall, this is consistent with previous studies (Bartoi et al., 2014; Bassilana et al., 1997). The abundance of heteromeric channels was even more apparent when using mutant mASIC1a subunits. For example, oocytes injected with only $1a^{G10′A}$ cRNA showed no responses to pH as low as 5.0, whereas 1:1 $1a^{G10′A}/2a^{WT}$-injected oocytes showed robust, monophasic responses to pH around 5.0 (Fig. 4 B), indicative of heteromeric channels carrying mutations in 1a subunits ($1a^{G10′A}/2a^{WT}$). The precise stoichiometry of heteromeric trimers is unclear, but we assume a mix of 1a/1a/2a and 1a/2a/2a, based on the flexible
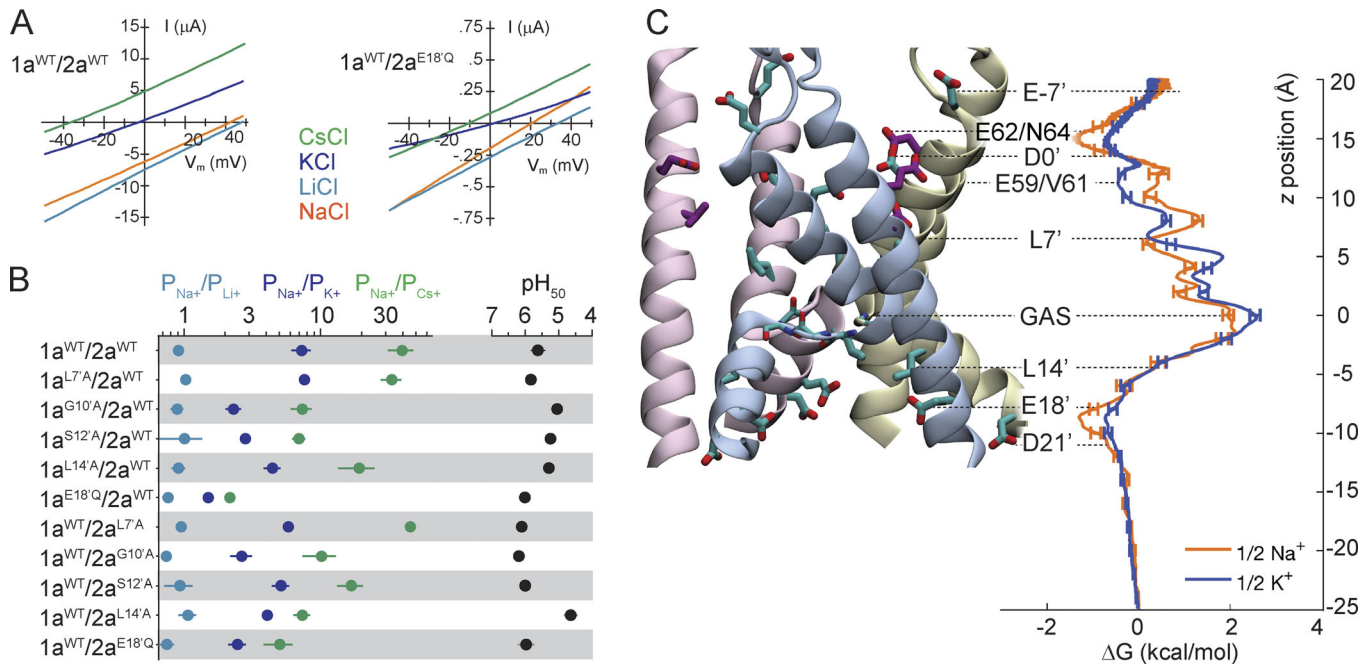
Figure 5. **Effects of M2 mutations on ion selectivity and MD simulations with ASIC1a/ASIC2a heteromers. (A)** Examples of pH 5.0–gated current through WT and mutant heteromeric channels in single oocytes. **(B)** Relative permeability ratios (P_{Na^+}/P_{X^+}) and half-maximal pH for activation (pH_{50}) for WT and mutant ASIC1a/ASIC2a heteromeric channels (mean ± SEM). **(C)** Single-ion free energy profiles for Na^+ (orange) and K^+ (blue) permeating the pore of the ASIC1/ASIC2 heteromer, with error bars represented by ±1 SEM.

stoichiometry previously demonstrated for WT heteromers (Bartoi et al., 2014).

These experiments show that pH 5.0 activates predominantly heteromeric channels in oocytes expressing mASIC1a and rASIC2a subunits, whether WT or mutant. To test ion selectivity of heteromeric ASICs, we therefore measured relative permeability when activating with pH 5.0. Under these conditions, $1a^{WT}/2a^{WT}$ heteromers showed ion selectivity (e.g., $P_{Na^+}/P_{K^+} = 7.4 ± 0.6$, $n = 4$; Fig. 5, A and B) similar to that reported previously (Bassilana et al., 1997). In heteromers carrying L7′A mutations in either the mASIC1a or rASIC2a subunit, ion selectivity was similar to WT heteromers (Fig. 5 B), reflecting the result at rASIC2a homomers, where the L7′A mutation had no effect on selectivity. The E18′Q mutation caused substantial decrease in selectivity in the heteromers, whether in the mASIC1a or rASIC2a subunit, without completely collapsing the relative permeability sequence of $P_{Na^+} ≈ P_{Li^+} > P_{K^+} > P_{Cs^+}$ (Fig. 5 B). This reflects results with concatemeric mASIC1a constructs containing one to two E18′Q mutations (Lynagh et al., 2017a), further indicative of a conserved role of E18′ in ion selectivity throughout different ASIC subtypes.

The expression of heteromers containing G10′A and S12′A mutations allowed us to test the contribution of these positions to ion selectivity, as these mutations render mASIC1a and rASIC2a homomers nonfunctional (Fig. 4 B). In mASIC1a subunits, and to a lesser extent in rASIC2a subunits, both the G10′A and S12′A mutations decreased ion selectivity of heteromers, although not as markedly as the E18′Q mutation (Fig. 5 B). This differs from results with concatemeric mASIC1a channels, in which one to two S12′A mutations had no effect on selectivity

(Lynagh et al., 2017a), providing further evidence that ASIC2a subunits shift the energy barrier from L7′ and the upper pore to the GAS belt. Finally, the L14′A mutation had relatively little effect on the selectivity of heteromers, tentatively suggesting that one to two L14′-containing subunits (WT subunits in heteromers) are sufficient to maintain appropriate lower pore conformation for selective Na^+ conduction.

We next performed MD simulations for Na^+ and K^+ permeating the heteromeric channels (mASIC1a/mASIC1a/rASIC2a and mASIC1a/rASIC2a/rASIC2a). These two heteromeric combinations were combined in equal proportions in Fig. 5 C by averaging the free energy profiles to reflect experiments with unknown stoichiometry (with separate profiles provided in Fig. S5 as reference). The free energy profiles in Fig. 5 C are similar to those for cASIC1 and rASIC2a (Fig. 3 A), being intermediate in nature, as illustrated in the direct comparison provided in Fig. S10. The free energy profiles of the heteromeric channels exhibit binding in the lower pore around E18′ and D21′, where we see an energetic preference for Na^+ over K^+, reflecting results for the homomers (Fig. 3 A). Similar to cASIC1 and rASIC2a homomers, this can be attributed to increased protein coordination for Na^+ by conserved E18′ side chains (Fig. S8). Furthermore, the slope seen above the GAS belt in rASIC2a (decrease in free energy from GAS toward the upper end of the pore due to long-ranged attractive interactions with rASIC2a E59 and E62) is also present in the heteromeric channels. This again leads the GAS belt to form the highest barrier to conduction for both Na^+ and K^+ ions (Fig. 5 C), decreasing the apparent importance of L7′. Despite a slight preference for Na^+ visible in the L7′ region in Fig. 5 C, such an

energetic difference may have little impact on permeation if this is not the rate-determining barrier. This is consistent with our experiments, as L7′A-containing heteromers showed relative permeability profiles much like WT, in contrast to some other mutant-containing heteromers (Fig. 5 B). In the same manner as in the ASIC2a homomer, both Na+ and K+ encounter wells around E59/V60, E62/E63, and D0′, driven by the long-ranged attractive electric fields (refer to potential maps in Fig. 3 C). As expected, the wells encountered in the heteromeric channels are less deep than those in rASIC2a, but larger than those in cASIC1 (Fig. S5). This region again favors Na+, owing to the stronger binding of the smaller cation to those carboxylate groups, evidenced by slightly increased protein coordination in Fig. S8 (although less striking than is the case in homomeric channels).

Discussion

ASICs occur as homomeric or heteromeric channels comprised of ASIC1a, -1b, -2a, -2b, -3, and/or -4 subunits. We set out to establish if the mechanism of ion selectivity in ASIC2a homomers and ASIC1a/ASIC2a heteromers reflects that observed for homomeric ASIC1a, the only isoform that had previously been studied in detail. In all channels tested, there exists a strong contribution to ion selectivity from conserved E18′ residues at the lower end of the pore. The E18′Q mutation abolishes or decreases selectivity in all channels tested, and MD free energy simulations again suggest a preference for Na+ over K+ in this lower part of the channel in ASIC2a homomers and ASIC1a/ASIC2a heteromers. Our MD simulations did show, however, that the free energy landscapes for ions in the upper half of the ASIC2a channel pore differ from ASIC1a channels, due to ASIC2a-specific acidic residues at the top of the channel. These glutamate residues create long-ranged electric fields that lower the energy of ions around the conserved L7′ residue in the upper half of the ASIC2a channel, relative to the conserved GAS belt in the middle of the channel, which appears to exhibit the largest barriers in ASIC2a-containing channels. In contrast, ASIC1a lacks these glutamate residues, leading to larger energy barriers at L7′, which we have suggested may be rate-determining for K+. This was reflected in our electrophysiology/mutagenesis experiments, where the L7′A mutation had no effect on ion selectivity in ASIC2a-containing channels but abolished selectivity in ASIC1a homomers.

Conserved determinants of channel function in the lower half of the ASIC pore

E18′ side chains, together with D21′, form a band of negatively charged carboxylates at the lower end of the ASIC pore. This engenders energetic preferences of 1–2 kcal/mol for Na+ over K+ in simulations with ASIC1a and ASIC2a homomers and ASIC1a/ASIC2a heteromers based on the PDB accession no. 4NTW template, despite a pore radius of ~8 Å in this part of the pore. We previously observed that, although selective Na+ binding to E18′/D21′ is exhibited regardless of the lower pore structure, the degree of selective Na+ binding is strongly influenced by it. In a closed-channel cASIC1 structure with a much

narrower pore (PDB accession no. 2QTS; Jasti et al., 2007), not only is the preference for single Na+ ions increased to ~3 kcal/mol, but multi-ion/multicarboxylate complexes occur far more frequently (especially for Na+), as E18′ and/or D21′ side chains from adjacent subunits are in much closer proximity. However, recent cryo-EM structural data of full-length cASIC1 show a splayed lower pore, similar to that observed in x-ray structural data on N- and C-terminal truncated cASIC1 (albeit with slightly reduced diameter). Nonetheless, this site has again demonstrated selective binding for Na+ ions at the channel's lower entrance that would be expected to facilitate permeation.

The role of L14′ in ion selectivity may also be conserved in different ASIC subtypes. Its substitution with Ala strongly decreases selectivity in ASIC1a and ASIC2a, although in heteromers containing presumably only one or two L14′A mutations, ion selectivity is intact. As L14′ side chains are oriented toward adjacent M2 helices in PDB accession no. 4NTW (Baconguis et al., 2014), we postulate that the L14′A mutation affects ion selectivity by disrupting inter-subunit interactions that maintain lower pore structure. A conserved role for L14′ in structural transitions of the channel is supported by our measurements of the potency of protons in activating the channels. Shifts in pH50 upon L14′I and L14′A mutations were observed for both ASIC1a and ASIC2a. (This is also the case for L7′ mutations, described below.) L14′ and E18′ are both highly conserved in the ASIC and broader degenerin (DEG)/ENaC family. Although few ASICs diverge at the E18′ position, three such subunits have been functionally tested. Toadfish ASIC2 channels containing A18′ were expressed in oocyte membranes but showed no proton-gated currents (Coric et al., 2005), reflecting results of the E18′A mutation in mASIC1a, which abolished channel activity (Lynagh et al., 2017a). Sea urchin and acorn worm ASIC subunits possessing a Q18′ residue and from a distinct subclade of ASICs showed low Na+/K+ selectivity (Lynagh et al., 2018), reflecting results of E18′Q mutations in mASIC1a and rASIC2a.

Differences between ASIC subtypes in the upper half of the channel

The GAS belt is highly conserved in ASICs, and we show that this constriction in the middle of the pore forms a large energy barrier to permeating ions in ASIC1a, ASIC2a, and ASIC1a/ASIC2a channels. We previously showed that in ASIC1a, the G10′ amide carbonyl group actually aids K+ permeation rather than selectively conducting Na+, and one or two S12′ mutations in concatemeric channels fail to alter selectivity (Lynagh et al., 2017a). However, and although the G10′ amide carbonyl was not amenable to amide-to-ester mutation in ASIC2a, our experiments with ASIC1a/ASIC2a heteromers suggest that the GAS belt could make a greater contribution to ion selectivity in ASIC2a-containing channels. We observed that one to two S12′A mutations caused a modest but noticeable decrease in selectivity of ASIC1a/ASIC2a heteromers. We also observed that in ASIC2a homomers, the L7′A mutation had no effect on ion selectivity, in stark contrast to ASIC1a, where this mutation abolished selectivity. Despite this, the L7′A mutation caused large increases in the potency with which protons activate both ASIC1a and ASIC2a (Lynagh et al., 2017a). This could originate from L7′ (and

possibly E59 near the thumb/wrist interface, whose mutation also increased potency) stabilizing a closed or nonconducting conformation of the protein, although our limited data on these positions are not sufficient to address this point in detail. In any case, the broadly conserved L7′ residue seems to play a conserved role in gating but makes different contributions to ion conduction in different ASIC subtypes.

MD free energy calculations of ion permeation through rASIC2a channels provide a possible explanation for these differences in ion selectivity for ASIC subtypes. In all ASICs we examined, the GAS belt forms a large, 2-kcal/mol barrier to permeation of both Na^+ and K^+ ions. In cASIC1, L7′, just above the GAS belt, forms a similarly large barrier for K^+ (>2 kcal/mol), but not Na^+ (<1 kcal/mol), with the upper vestibule of the channel also maintaining a 1-kcal/mol barrier for both ions. This means that both species permeate similarly until L7′ on their path down the cASIC1 pore. In rASIC2a, however, carboxylate side chains from M1 glutamate residues (E59 and E62), together with conserved D0′ residues, create an energetic minimum in the upper pore (approximately –2 kcal/mol for Na^+ and approximately –1.2 kcal/mol for K^+), from which free energy gradually increases past L7′ (0 kcal/mol for both species), peaking at the GAS belt (∼2.2 kcal/mol for both ionic species; Fig. 3 A). Thus, the upper carboxylates, specific to rASIC2a, seem to ease ions past L7′, bringing the GAS belt more into play than in cASIC1. This could potentially help explain the effects of G10′A and S12′A mutations on ion selectivity in rASIC2a-containing heteromers. We had hypothesized from this that the off-axis E59/E62 carboxylate charges would affect conduction of both Na^+ and K^+ ions via their long-ranged electric fields (see Fig. 3 B), potentially eliminating sensitivity to changes at L7′ by making this site less rate-determining. However, we saw only a modest change when the same mutation was performed concurrently with elimination of those charges on the M1 glutamate residues. This suggests that those upper charges are not the only difference between the rASIC2a and cASIC1 channels affecting conduction. Subsequent analysis revealed that the upper pore in the rASIC2a model was wider than cASIC1, leading to reduced ion dehydration, and that the L7′ location in the WT rASIC2a channel had reduced the difference in free energy of the K^+ and Na^+ ions. We conclude from these observations that, although mutation of upper charges would perturb the shape of the free energy profile for ions in a way that could raise the energy near the L7′ site, other structural differences lead this site to be less thermodynamically selective. This explains the lack of effect of L7′ mutation in the rASIC2a channel. We do concede, however, that the dramatic differences in experimental L7′ mutant effects on mASIC1a and rASIC2a selectivity are unexpected given the small structural differences between cASIC1 and our model of rASIC2a based on the cASIC1 structure.

Our study, covering different ASIC subtypes, has refined the contributions of multiple sites of interest for understanding ion selectivity in this subfamily of the ENaC/DEG superfamily. This includes the conserved contributions of carboxylate-containing side chains in the lower pore (E18′/D21′), as well as residues at or near the central constriction, involving the GAS belt or the neighboring L7′ in ASIC2a and ASIC1a-containing channels,

respectively. Additionally, ion selectivity is likely modulated electrostatically by species-dependent sequence differences in the upper pore. However, our functional work was limited to reversal potentials and relative permeability, so we cannot exclude contributions of some of these and other residues to relative ion conduction and thus selectivity. Future work should address this aspect, perhaps especially regarding the residues in the upper pore, whose mutation had little effect on relative ion permeability. Finally, our work has established ASIC heteromer expression as a powerful tool to functionally test mutants that render homomeric channels nonfunctional, thus providing mechanistic insight on all key regions of the pore contributing to Na^+ selectivity across the ASIC family.

Acknowledgments

References

Allen, T.W., O.S. Andersen, and B. Roux. 2004. On the importance of atomic fluctuations, protein flexibility, and solvent in ion permeation. *J. Gen. Physiol.* 124:679–690. https://doi.org/10.1085/jgp.200409111

Allen, T.W., O.S. Andersen, and B. Roux. 2006. Molecular dynamics - potential of mean force calculations as a tool for understanding ion permeation and selectivity in narrow channels. *Biophys. Chem.* 124:251–267. https://doi.org/10.1016/j.bpc.2006.04.015

Andersen, H.C. 1980. Molecular dynamics simulations at constant pressure and/or temperature. *J. Chem. Phys.* 72:2384–2393. https://doi.org/10.1063/1.439486

Andersen, H.C. 1983. Rattle: A "velocity" version of the shake algorithm for molecular dynamics calculations. *J. Comput. Phys.* 52:24–34. https://doi.org/10.1016/0021-9991(83)90014-1

Baconguis, I., and E. Gouaux. 2012. Structural plasticity and dynamic selectivity of acid-sensing ion channel-spider toxin complexes. *Nature.* 489:400–405. https://doi.org/10.1038/nature11375

Baconguis, I., C.J. Bohlen, A. Goehring, D. Julius, and E. Gouaux. 2014. X-ray structure of acid-sensing ion channel 1-snake toxin complex reveals open state of a Na(+)-selective channel. *Cell.* 156:717–729. https://doi.org/10.1016/j.cell.2014.01.011

Bartoi, T., K. Augustinowski, G. Polleichtner, S. Gründer, and M.H. Ulbrich. 2014. Acid-sensing ion channel (ASIC) 1a/2a heteromers have a flexible 2:1/1:2 stoichiometry. *Proc. Natl. Acad. Sci. USA.* 111:8281–8286. https://doi.org/10.1073/pnas.1324060111

Bassilana, F., G. Champigny, R. Waldmann, J.R. de Weille, C. Heurteaux, and M. Lazdunski. 1997. The acid-sensitive ionic channel subunit ASIC and the mammalian degenerin MDEG form a heteromultimeric H+-gated Na+ channel with novel properties. *J. Biol. Chem.* 272:28819–28822. https://doi.org/10.1074/jbc.272.46.28819

Bernèche, S., and B. Roux. 2001. Energetics of ion conduction through the K+ channel. *Nature.* 414:73–77. https://doi.org/10.1038/35102067

Brooks, B.R., R.E. Bruccoleri, B.D. Olafson, D.J. States, S. Swaminathan, and M. Karplus. 1983. CHARMM: A program for macromolecular energy, minimization, and dynamics calculations. *J. Comput. Chem.* 4(2):187–217.

Brooks, B.R., C.L. Brooks, III, A.D. Mackerell, Jr., L. Nilsson, R.J. Petrella, B. Roux, Y. Won, G. Archontis, C. Bartels, S. Boresch, et al. 2009. CHARMM: The biomolecular simulation program. *J. Comput. Chem.* 30(10):1545–1614.

Carattino, M.D., and M.C. Della Vecchia. 2012. Contribution of residues in second transmembrane domain of ASIC1a protein to ion selectivity. *J. Biol. Chem.* 287:12927–12934. https://doi.org/10.1074/jbc.M111.329284

Coric, T., D. Zheng, M. Gerstein, and C.M. Canessa. 2005. Proton sensitivity of ASIC1 appeared with the rise of fishes by changes of residues in the region that follows TM1 in the ectodomain of the channel. *J. Physiol.* 568:725–735. https://doi.org/10.1113/jphysiol.2005.087734

Dahan, D.S., M.I. Dibas, E.J. Petersson, V.C. Auyeung, B. Chanda, F. Bezanilla, D.A. Dougherty, and H.A. Lester. 2004. A fluorophore attached to nicotinic acetylcholine receptor beta M2 detects productive binding of agonist to the alpha delta site. *Proc. Natl. Acad. Sci. USA.* 101:10195–10200. https://doi.org/10.1073/pnas.0301885101

Feller, S.E., Y. Zhang, R.W. Pastor, and B.R. Brooks. 1995. Constant pressure molecular dynamics simulation: The Langevin piston method. *J. Chem. Phys.* 103:4613–4621. https://doi.org/10.1063/1.470648

Flood, E., et al. 2019. Atomistic Simulations of Membrane Ion Channel Conduction, Gating, and Modulation. *Chemical Reviews.* 119(13):7737–7832. https://doi.org/10.1021/acs.chemrev.8b00630

Grabe, M., D. Bichet, X. Qian, Y.N. Jan, and L.Y. Jan. 2006. K+ channel selectivity depends on kinetic as well as thermodynamic factors. *Proc. Natl. Acad. Sci. USA.* 103:14361–14366. https://doi.org/10.1073/pnas.0606662103

Gründer, S., and M. Pusch. 2015. Biophysical properties of acid-sensing ion channels (ASICs). *Neuropharmacology.* 94:9–18. https://doi.org/10.1016/j.neuropharm.2014.12.016

Hoover, W.G. 1985. Canonical dynamics: Equilibrium phase-space distributions. *Phys. Rev. A Gen. Phys.* 31:1695–1697. https://doi.org/10.1103/PhysRevA.31.1695

Im, W., D. Beglov, and B. Roux. 1998. Continuum solvation model: computation of electrostatic forces from numerical solutions to the Poisson-Boltzmann equation. *Comput. Phys. Commun.* 111:59–75. https://doi.org/10.1016/S0010-4655(98)00016-2

Jasti, J., H. Furukawa, E.B. Gonzales, and E. Gouaux. 2007. Structure of acid-sensing ion channel 1 at 1.9 A resolution and low pH. *Nature.* 449:316–323. https://doi.org/10.1038/nature06163

Jorgensen, W.L., J. Chandrasekhar, J.D. Madura, R.W. Impey, and M.L. Klein. 1983. Comparison of simple potential functions for simulating liquid water. *The Journal of Chemical Physics.* 79(2):926–935.

Kellenberger, S., and L. Schild. 2015. International Union of Basic and Clinical Pharmacology. XCI. structure, function, and pharmacology of acid-sensing ion channels and the epithelial Na+ channel. *Pharmacol. Rev.* 67:1–35. https://doi.org/10.1124/pr.114.009225

Kellenberger, S., I. Gautschi, and L. Schild. 1999. A single point mutation in the pore region of the epithelial Na+ channel changes ion selectivity by modifying molecular sieving. *Proc. Natl. Acad. Sci. USA.* 96:4170–4175. https://doi.org/10.1073/pnas.96.7.4170

Klauda, J.B., R.M. Venable, J.A. Freites, J.W. O'Connor, D.J. Tobias, C. Mondragon-Ramirez, I. Vorobyov, A.D. MacKerell, Jr., and R.W. Pastor. 2010. Update of the CHARMM All-Atom Additive Force Field for Lipids: Validation on Six Lipid Types. *J. Phys. Chem. B.* 114(23):7830–7843.

Kumar, S., J.M. Rosenberg, D. Bouzida, R.H. Swendsen, and P.A. Kollman. 1992. THE weighted histogram analysis method for free-energy calculations on biomolecules. I. The method. *J. Comput. Chem.* 13:1011–1021. https://doi.org/10.1002/jcc.540130812

Li, T., Y. Yang, and C.M. Canessa. 2011. Outlines of the pore in open and closed conformations describe the gating mechanism of ASIC1. *Nat. Commun.* 2:399. https://doi.org/10.1038/ncomms1409

Lynagh, T., E. Flood, C. Boiteux, M. Wulf, V.V. Komnatnyy, J.M. Colding, T.W. Allen, and S.A. Pless. 2017a. A selectivity filter at the intracellular end of the acid-sensing ion channel pore. *eLife.* 6:e24630. https://doi.org/10.7554/eLife.24630

Lynagh, T., V.V. Komnatnyy, and S.A. Pless. 2017b. Unique Contributions of an Arginine Side Chain to Ligand Recognition in a Glutamate-gated Chloride Channel. *J. Biol. Chem.* 292:3940–3946. https://doi.org/10.1074/jbc.M116.772939

Lynagh, T., Y. Mikhaleva, J.M. Colding, J.C. Glover, and S.A. Pless. 2018. Acid-sensing ion channels emerged over 600 Mya and are conserved throughout the deuterostomes. *Proc. Natl. Acad. Sci. USA.* 115:8430–8435. https://doi.org/10.1073/pnas.1806614115

Mackerell, A.D., Jr., M. Feig, and C.L. Brooks, III. 2004. Extending the treatment of backbone energetics in protein force fields: Limitations of gas-phase quantum mechanics in reproducing protein conformational distributions in molecular dynamics simulations. *J. Comput. Chem.* 25(11):1400–1415.

MacKerell, A.D., Jr., D. Bashford, M. Bellott, R.L. Dunbrack, Jr., J.D. Evanseck, M.J. Field, S. Fischer, J. Gao, H. Guo, S. Ha, et al. 1998. All-Atom Empirical Potential for Molecular Modeling and Dynamics Studies of Proteins†. *J. Phys. Chem. B.* 102(18):3586–3616.

Marinelli, F., L. Almagor, R. Hiller, M. Giladi, D. Khananshvili, and J.D. Faraldo-Gómez. 2014. Sodium recognition by the Na+/Ca2+exchanger in the outward-facing conformation. *Proc Natl Acad Sci USA.* 111(50):E5354–E5362.

Nina, M., D. Beglov, and B. Roux. 1997. Atomic radii for continuum electrostatics calculations based on molecular dynamics free energy simulations. *J. Phys. Chem. B.* 101:5239–5248. https://doi.org/10.1021/jp970736r

Nosé, S. 1984. A unified formulation of the constant temperature molecular dynamics methods. *J. Chem. Phys.* 81:511–519. https://doi.org/10.1063/1.447334

Noskov, S.Y., and B. Roux. 2008. Control of Ion Selectivity in LeuT: Two Na+ Binding Sites with Two Different Mechanisms. *Journal of Molecular Biology.* 377(3):804–818.

Noskov, S.Y., S. Bernèche, and B. Roux. 2004. Control of ion selectivity in potassium channels by electrostatic and dynamic properties of carbonyl ligands. *Nature.* 431:830–834. https://doi.org/10.1038/nature02943

Paukert, M., S. Sidi, C. Russell, M. Siba, S.W. Wilson, T. Nicolson, and S. Gründer. 2004. A family of acid-sensing ion channels from the zebrafish: widespread expression in the central nervous system suggests a conserved role in neuronal communication. *J. Biol. Chem.* 279:18783–18791. https://doi.org/10.1074/jbc.M401477200

Phillips, J.C., R. Braun, W. Wang, J. Gumbart, E. Tajkhorshid, E. Villa, C. Chipot, R.D. Skeel, L. Kalé, and K. Schulten. 2005. Scalable molecular dynamics with NAMD. *J. Comput. Chem.* 26(16):1781–1802.

Roux, B. 2010. Exploring the ion selectivity properties of a large number of simplified binding site models. *Biophys. J.* 98:2877–2885. https://doi.org/10.1016/j.bpj.2010.03.038

Ryckaert, J.-P., G. Ciccotti, and H.J.C. Berendsen. 1977. Numerical integration of the cartesian equations of motion of a system with constraints: molecular dynamics of n-alkanes. *J. Comput. Phys.* 23:327–341. https://doi.org/10.1016/0021-9991(77)90098-5

Smart, O.S., J.G. Neduvelil, X. Wang, B.A. Wallace, and M.S. Sansom. 1996. HOLE: a program for the analysis of the pore dimensions of ion channel structural models. *J. Mol. Graph.* 14:354–360. https://doi.org/10.1016/S0263-7855(97)00009-X

Torrie, G.M., and J.P. Valleau. 1977. Nonphysical sampling distributions in Monte Carlo free-energy estimation: Umbrella sampling. *J. Comput. Phys.* 23:187–199. https://doi.org/10.1016/0021-9991(77)90121-8

Waldmann, R., G. Champigny, F. Bassilana, C. Heurteaux, and M. Lazdunski. 1997. A proton-gated cation channel involved in acid-sensing. *Nature.* 386:173–177. https://doi.org/10.1038/386173a0

Wemmie, J.A., R.J. Taugher, and C.J. Kreple. 2013. Acid-sensing ion channels in pain and disease. *Nat. Rev. Neurosci.* 14:461–471. https://doi.org/10.1038/nrn3529

Yang, L., and L.G. Palmer. 2014. Ion conduction and selectivity in acid-sensing ion channel 1. *J. Gen. Physiol.* 144:245–255. https://doi.org/10.1085/jgp.201411220

Yang, L., and L.G. Palmer. 2018. Determinants of selective ion permeation in the epithelial Na+ channel. *J. Gen. Physiol.* 150:1397–1407. https://doi.org/10.1085/jgp.201812164

Yang, H., Y. Yu, W.G. Li, F. Yu, H. Cao, T.L. Xu, and H. Jiang. 2009. Inherent dynamics of the acid-sensing ion channel 1 correlates with the gating mechanism. *PLoS Biol.* 7:e1000151. https://doi.org/10.1371/journal.pbio.1000151

Yoder, N., C. Yoshioka, and E. Gouaux. 2018. Gating mechanisms of acid-sensing ion channels. *Nature.* 555:397–401. https://doi.org/10.1038/nature25782
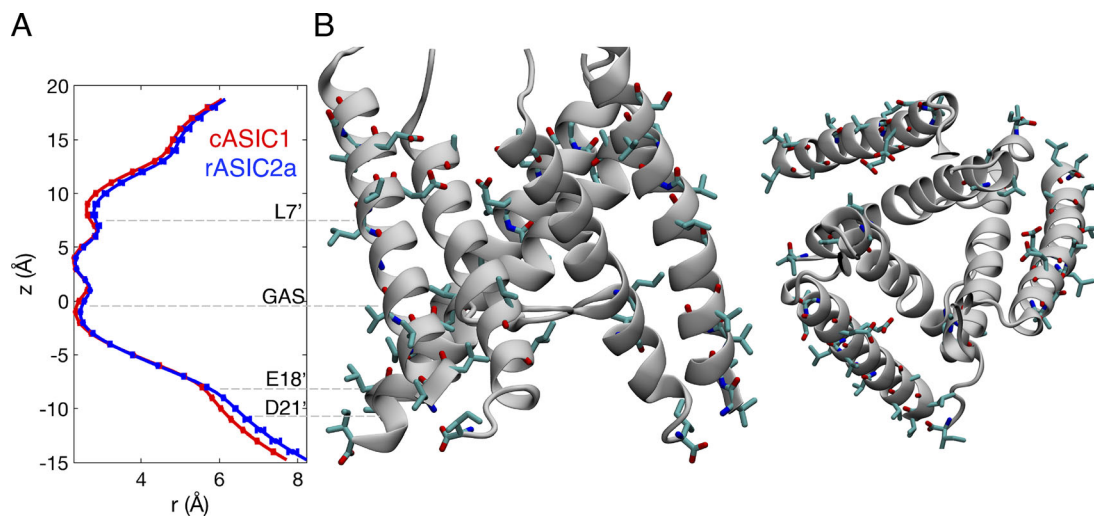
Figure S1. **Differences in the structures of cASIC1 and rASIC2a. (A)** Pore size for cASIC1 (red) and equilibrated rASIC2a model (blue) calculated using HOLE (Smart et al., 1996), based on the last 100 ns of each simulation, with error bars based on SEMs from five blocks. Positions of L7', GAS, and E18'/D21' are indicated with dashed lines. **(B)** Divergent residues in rASIC2a (corresponding residue names and numbers can be seen in the sequence alignment in Fig. 1).
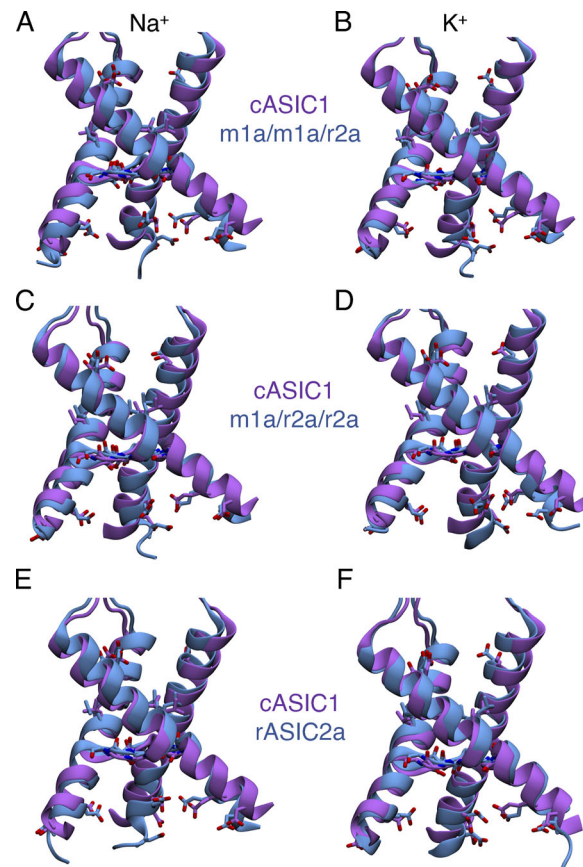
Figure S2. **Structural alignments of M2 helices. (A–F)** Structural alignments of M2 helices between cASIC1 crystal structure (purple) and mASIC1a/mASIC1a/rASIC2a heteromers (blue) for Na⁺ (left) and K⁺ (right; A and B), mASIC1a/rASIC2a/rASIC2a heteromers (blue; C and D), and rASIC2a homomers (blue; E and F) after 100-ns simulation. The alignment reveals close agreement between the original structure and the homology models, albeit with small deviations at the ends of the M2 helices due to truncation of the PDB structure in this solvent-exposed region. In particular, unfolding of residues 22′ and 23′ can be seen in at least one of the three subunits in all channels.
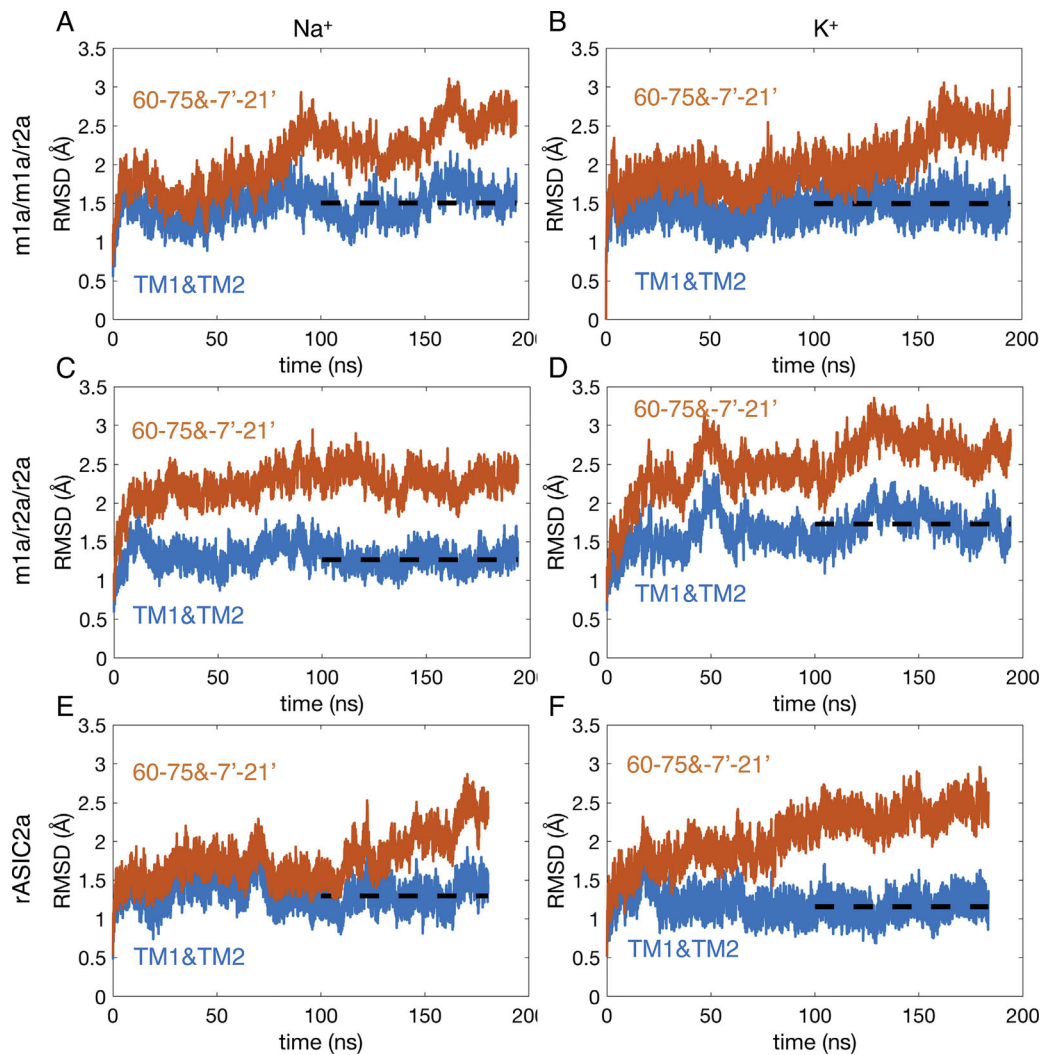
Figure S3. **RMSD for the backbone of TM1 and TM2 (residues 45 to 75 and 425 to 456 in red, and residues 60 to 75 and 425 to 454 in blue; PDB accession no. 4NTW numbering). (A and B)** mASIC1a/mASIC1a/rASIC2a heteromers with NaCl (A) and KCl (B). **(C and D)** mASIC1a/rASIC2a/rASIC2a heteromers with NaCl (C) and KCl (D). **(E and F)** rASIC2a with NaCl (E) and KCl (F).
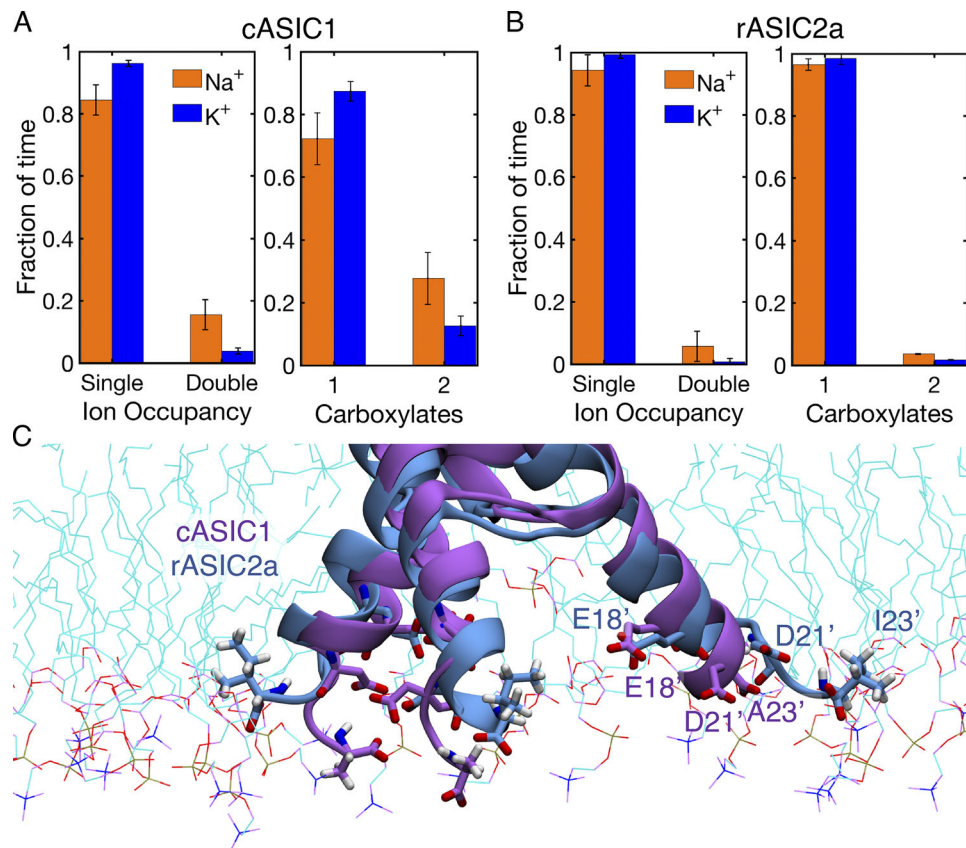
Figure S4. **Behavior of the lower pore of cASIC1 and rASIC2a. (A and B)** Distribution of single and double occupancy for sites formed by E18′ and D21′ for cASIC1 (A) and rASIC2a (B) channels (mean ± SEM). Single ion occupancy is preferred in cASIC1 and rASIC2a for both Na$^+$ and K$^+$; however, double occupancy occurs more frequently for Na$^+$ than K$^+$. Single occupancy is more frequent both for Na$^+$ and K$^+$ in rASIC2a than cASIC1 (A and B; left graph). In the doubly occupied sites in cASIC1 and rASIC2a, both the Na$^+$ and K$^+$ ions are most often bound by a single carboxylate side chain; however, multicarboxylate complexes are more frequent for Na$^+$ than for K$^+$. Multicarboxylate sites are less frequent in rASIC2a than for cASIC1 (A and B; right graph). **(C)** Behavior of the end of TM2 for cASIC1 and rASIC2a. The large hydrophobic sidechain of I23′ in rASIC2a points up toward the lipids, while A23′ in cASIC1 points down toward water; this pulls D21′ away from E18′, and the likelihood of multicarboxylate clusters decreases.
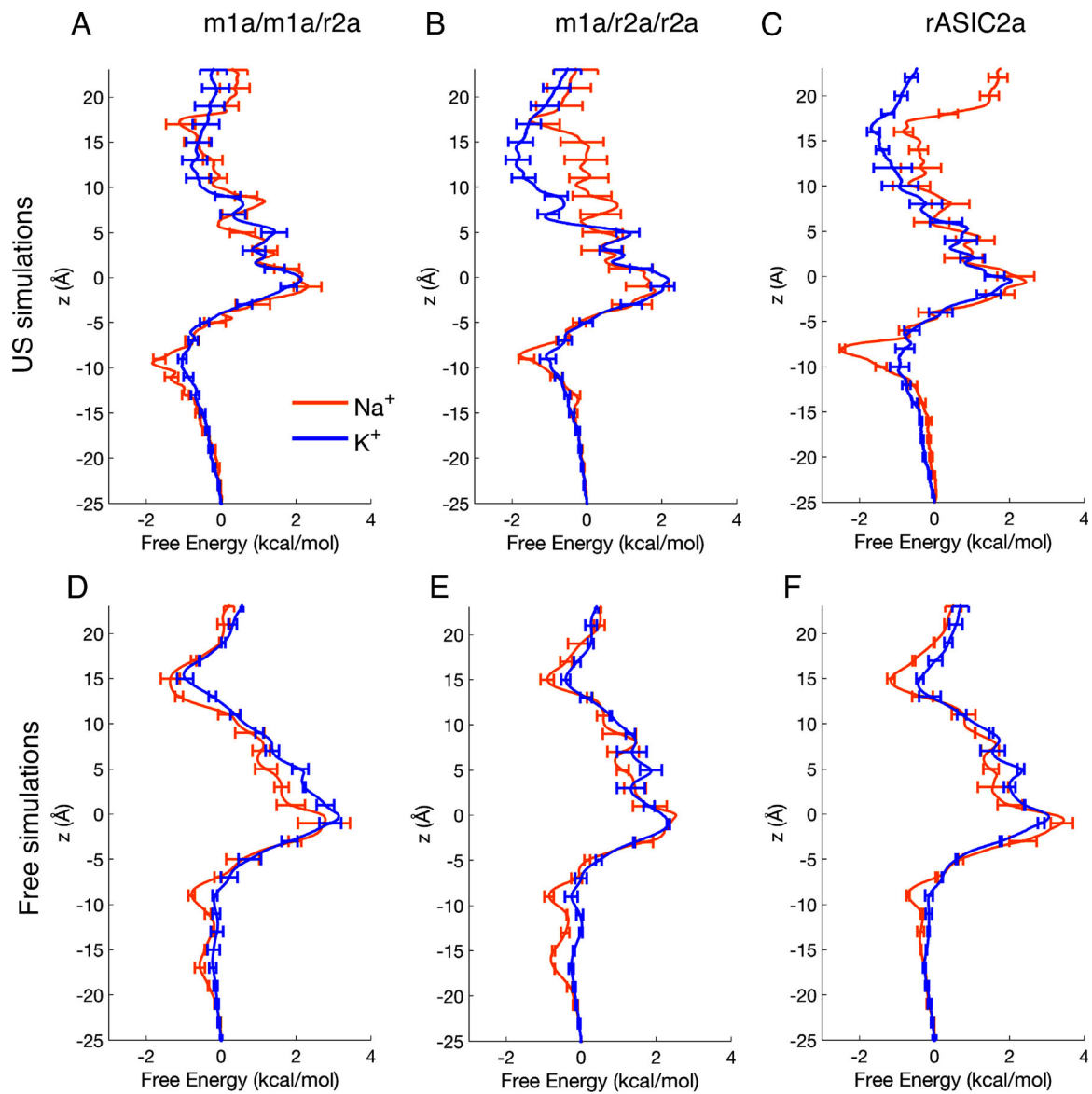
Figure S5. **PMFs for Na+ and K+. (A–F)** PMFs for Na+ (orange) and K+ (blue) permeating the pore of mASIC1a/mASIC1a/rASIC2a heteromers (A and D) from US simulations (A) and free simulations (D); mASIC1a/rASIC2a/rASIC2a heteromers (B and E) from US simulations (B) and free simulations (E); and rASIC2a (C and F) from US simulations (C) and free simulations (F). Error bars are represented by ±1 SEM.
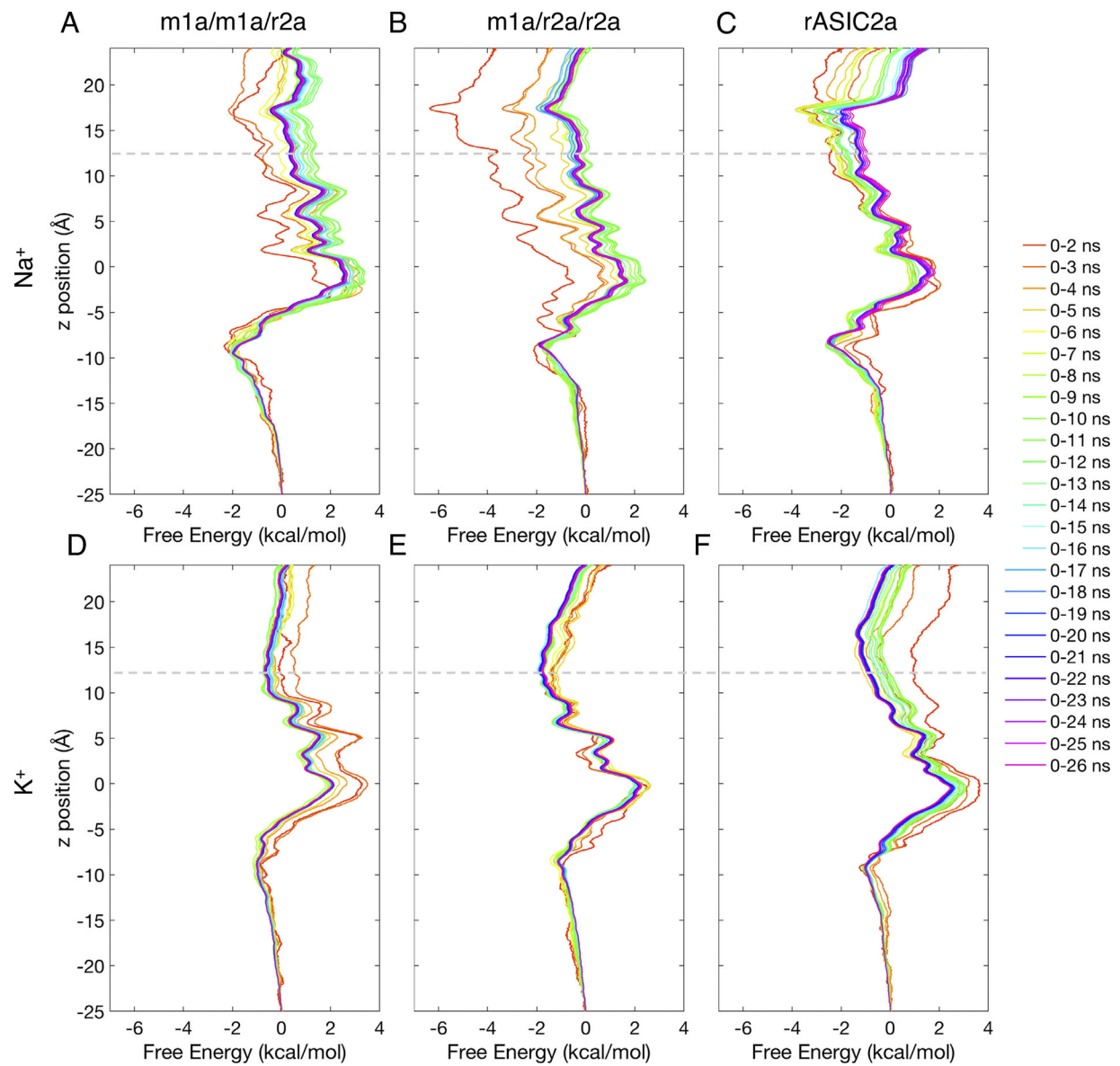
Figure S6. **Convergence of PMFs from US simulation. (A and D)** mASIC1a/mASIC1a/rASIC2a heteromers with Na⁺ (A) and K⁺ (D). **(B and E)** mASIC1a/rACIS2a/rASIC2a heteromers with Na⁺ (B) and K⁺ (E). **(C and F)** rASIC2a with Na⁺ (C) and K⁺ (F). Above the dotted line at z = 11 Å, there were convergence issues due to the wide pore and many charged residues (E/V59, E/N61, and D0'), and the US results were discarded; the PMF was based on free simulations in that region (see Materials and methods).
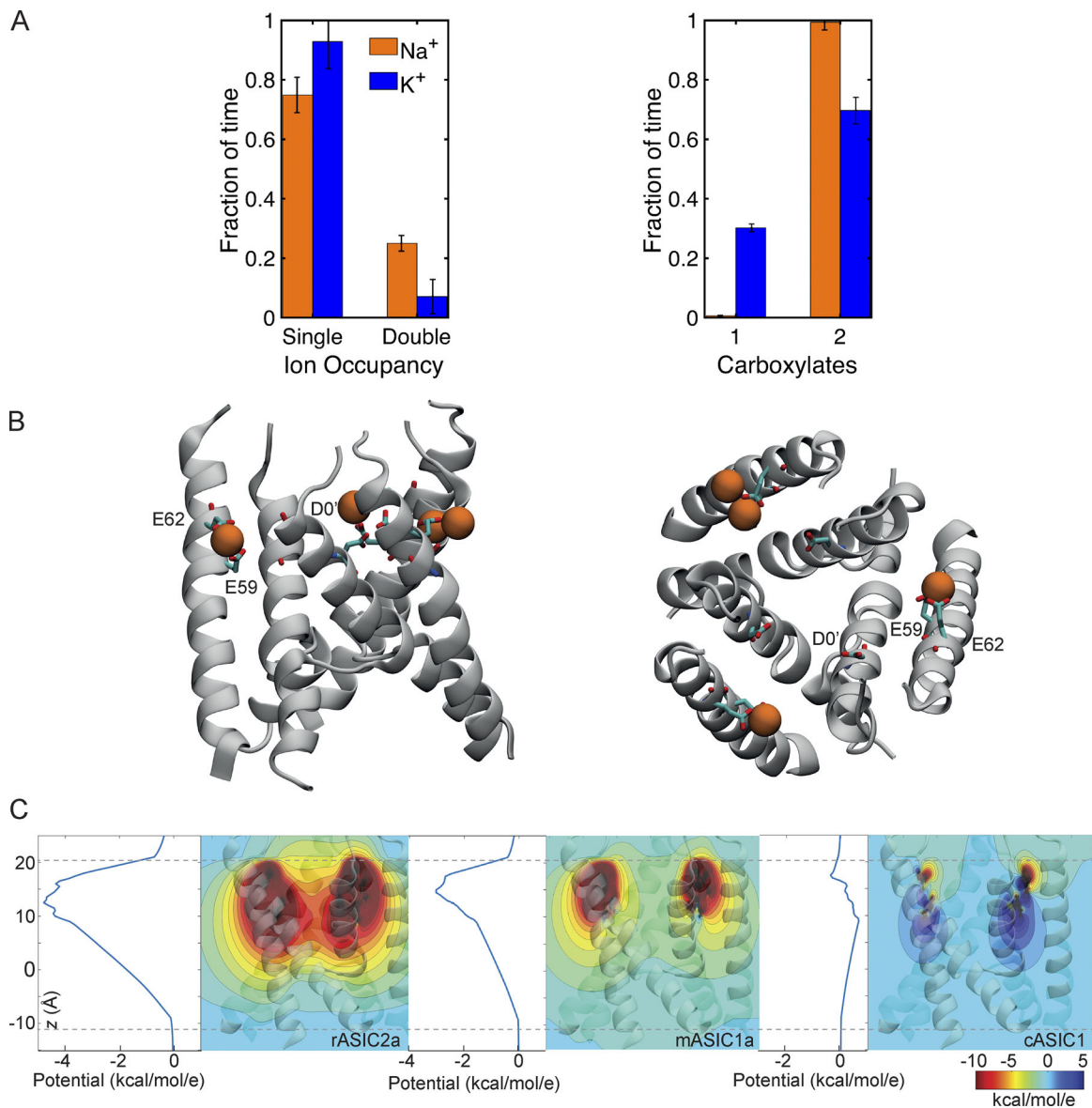
Figure S7. **Behavior of the upper pore of cASIC1 and rASIC2a. (A)** Distribution of single and double occupancy in rASIC2a in sites formed by E59, E62, and E0' showing occupancy and number of carboxylates (mean ± SEM). Single-ion occupancy is preferred for both Na$^+$ and K$^+$; however, double occupancy occurs more frequently for Na$^+$ than K$^+$ (left). In the doubly occupied sites, both Na$^+$ and K$^+$ prefer to be bound by multiple, rather than single, carboxylates, and Na$^+$ is almost solely bound by multiple carboxylates (right). **(B)** Typical Na$^+$ occupancy in these sites, viewed from the side (left) and above (right), showing how these sites are far from the permeation pathway. **(C)** Electrostatic potential from E59 and E62 in rASIC2a, V60 and E63 in mASIC1a, and V61 and N64 in cASIC1. The dotted lines indicate the position of the membrane.
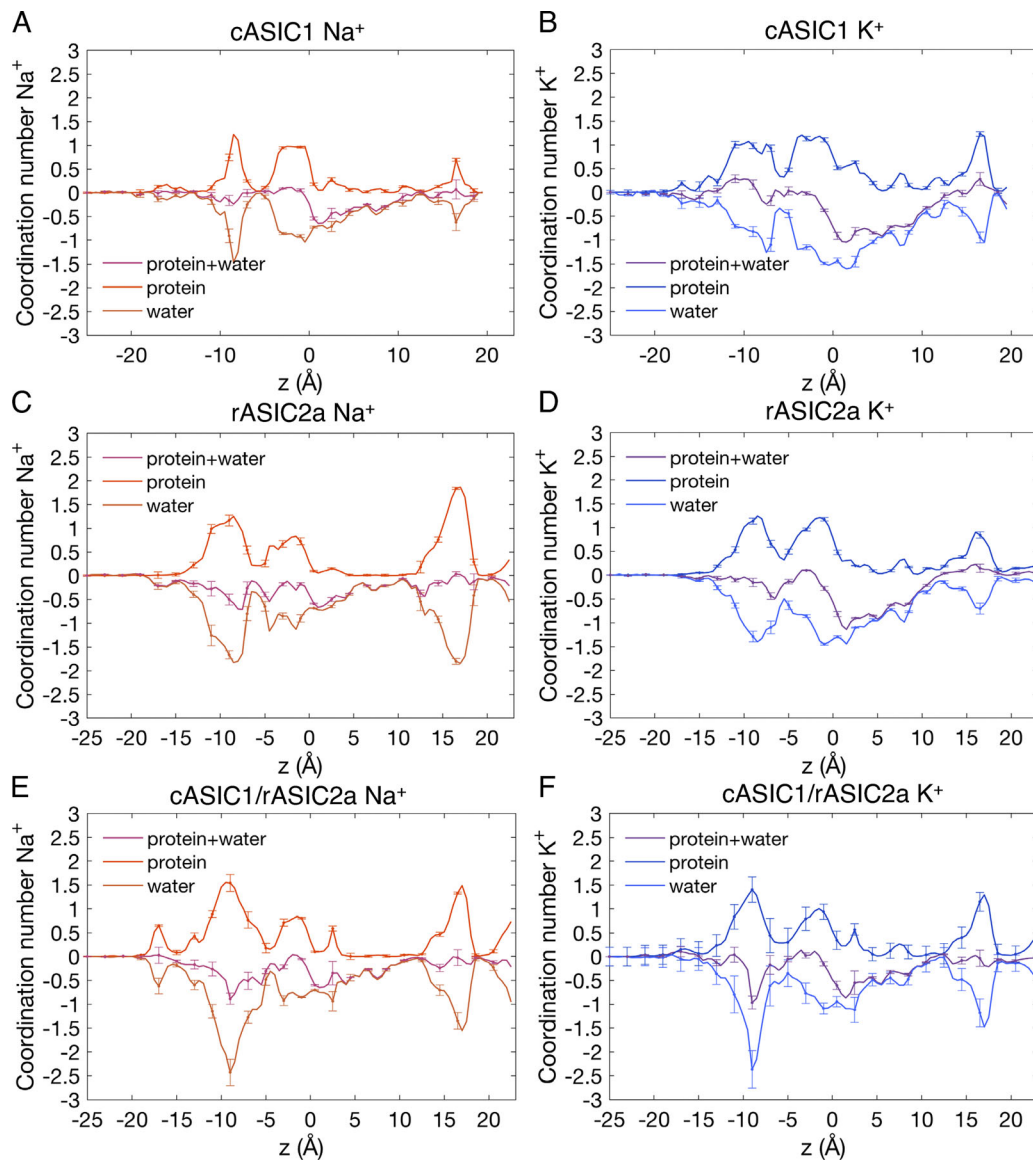
Figure S8. **First shell coordination by oxygen atoms from water and protein. (A and B)** cASIC1 pore for Na$^+$ (A) and K$^+$ (B). **(C and D)** rASIC2a pore for Na$^+$ (C) and K$^+$ (D). **(E and F)** mASIC1a/rASIC2a heteromer pore for (E) Na$^+$ and (F) K$^+$. Values plotted are mean ± SEM.
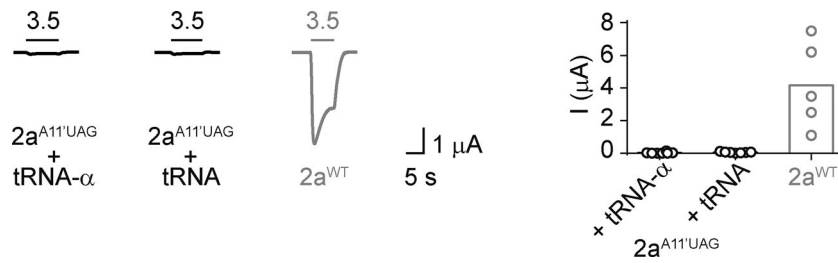
Figure S9.   **Lack of functional expression when replacing A11′ with lactic acid (α) in rASIC2a channels.** Previous work shows that coinjection of oocytes with mutant mASIC1a cRNA, containing the amber stop codon (UAG) instead of the A11′ codon, with hydroxyacylated *Tetrahymena thermophila* tRNA (tRNA-α) results in the expression of A11′α-containing channels (Lynagh et al., 2017). However, no currents were observed in response to pH 3.5 at oocytes coinjected with 46 ng rASIC2a A11′UAG cRNA and tRNA-α (n = 8, over three batches of oocytes) or with 46 ng ASIC2a A11′UAG cRNA and tRNA (n = 7; as a control for nonspecific incorporation of endogenous amino acids). In contrast, oocytes injected with 0.8 ng ASIC2a WT cRNA showed large inward currents in response to pH 3.5 on the same day of recording. Left, example recordings; right, means (columns) and individual data points.
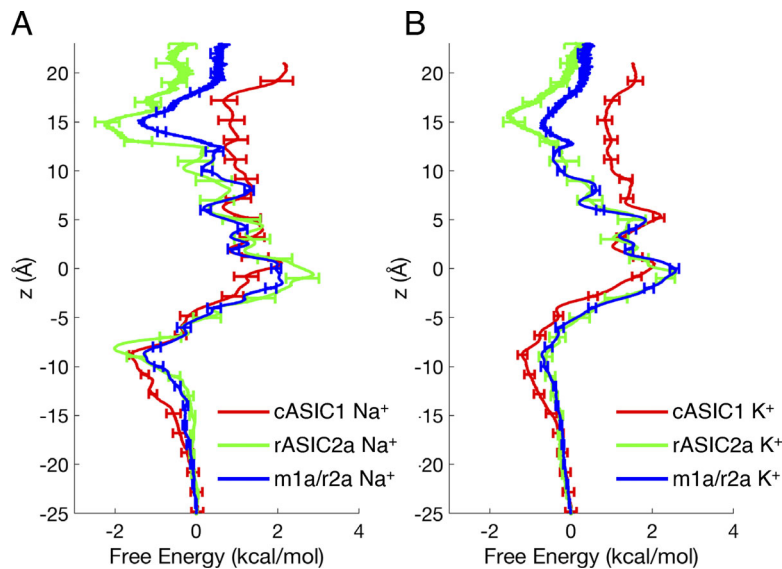

Figure S10.   **Comparison of the PMFs for cASIC1, rASIC2a, and mASIC1a/rASIC2a heteromers.** mASIC1a/rASIC2a is the average of mASIC1a/mASIC1a/rASIC2a and mASIC1a/rASIC2a/rASIC2a to reflect experiments, with error bars represented by ±1 SEM. **(A and B)** Na⁺ permeating the pore (A) and K⁺ permeating the pore (B).